AFRL-AFOSR-UK-TR-2012-0018

Hypersonic Transition Experiments in 3D Cone Flow with New Measurement Techniques

Dirk Heitmann
Rolf E. Radespiel

Technische Universitaet Braunschweig
Institut Fur Stromungsmechanik
Bienroder Weg 3
Braunschweig, Germany 38106

EOARD Grant 09-3014

Report Date: August 2012

Final Report for 15 April 2009 to 14 April 2012

Air Force Research Laboratory
Air Force Office of Scientific Research
European Office of Aerospace Research and Development
Unit 4515 Box 14, APO AE 09421

REPORT DOCUMENTATION PAGE

Form Approved OMB No. 0704-0188

1. REPORT DATE *(DD-MM-YYYY)*
14 August 2012

2. REPORT TYPE
Final Report

3. DATES COVERED *(From – To)*
15 April 2009 – 14 April 2012

4. TITLE AND SUBTITLE

Hypersonic Transition Experiments in 3D Cone Flow with New Measurement Techniques

5a. CONTRACT NUMBER

FA8655-09-1-3014

5b. GRANT NUMBER

Grant 09-3014

5c. PROGRAM ELEMENT NUMBER

61102F

6. AUTHOR(S)

Dirk Heitmann
Rolf E. Radespiel

5d. PROJECT NUMBER

5d. TASK NUMBER

5e. WORK UNIT NUMBER

7. PERFORMING ORGANIZATION NAME(S) AND ADDRESS(ES)
Technische Universitaet Braunschweig
Institut Fur Stromungsmechanik
Bienroder Weg 3
Braunschweig, Germany 38106

8. PERFORMING ORGANIZATION REPORT NUMBER

N/A

9. SPONSORING/MONITORING AGENCY NAME(S) AND ADDRESS(ES)

EOARD
Unit 4515 BOX 14
APO AE 09421

10. SPONSOR/MONITOR'S ACRONYM(S)

AFOSR/AFRL/RSW (EOARD)

11. SPONSOR/MONITOR'S REPORT NUMBER(S)

AFRL-AFOSR-UK-TR-2012-0018

12. DISTRIBUTION/AVAILABILITY STATEMENT

Approved for public release; distribution is unlimited.

13. SUPPLEMENTARY NOTES

14. ABSTRACT

This is the final report on the project with grant number FA8655-09-1-3014 dealing with laminar-turbulent transition measurements on an inclined cone at hypersonic Mach number. The report summarizes the main results reported in the last reports. Furthermore the work conducted within the last period of six months is described.

Within the flow field of an inclined cone three different boundary layer instabilities appear: first and second mode instability waves and crossflow vortices. Two different measurement techniques were applied for investigating them: (i) IR-thermography was used for measuring stationary crossflow vortices. This instability was quantitatively measured. The position where these vortices evolve, their amplification and their wavenumber were determined. Furthermore experiments were conducted aiming on affecting this wavenumber by placing small roughness elements on the cone surface that generate vortices. (ii) surface mounted pressure sensors were used for measuring travelling instabilities. The second mode waves are characterized regarding the position on the model where they appear, their frequency content and their spatial extensions and wave structure. Also low frequency waves (f ≈ 20-40 kHz) were detected. These waves are so far interpreted as first mode waves, but since no stability computations are available this is uncertain. Also travelling crossflow vortices might cause this signal.

The measurements of the wave structure and the spatial extent of second mode wave packets required an uncommon cone model. In total tree different model were used within this project. The last report covered the design of a new model with extended possibilities for mounting sensors. In the meantime new measurements have been conducted with this model and they are reported here. Measurements with suited positioning of pressure gauges and correlations of their signals allowed measurements of the spatial extent and propagation direction of second mode instability waves. Furthermore, the new experimental results indicate the presence of low frequency waves and by analysis of the acquired data with higher order spectra new insights into the nonlinear stage of the transition process could be obtained.

15. SUBJECT TERMS

EOARD, Aerodyanamics, Transition, Hypersonic Flow

16. SECURITY CLASSIFICATION OF:

a. REPORT	b. ABSTRACT	c. THIS PAGE	17. LIMITATION OF ABSTRACT	18, NUMBER OF PAGES
UNCLAS	UNCLAS	UNCLAS	SAR	40

19a. NAME OF RESPONSIBLE PERSON
Gregg Abate

19b. TELEPHONE NUMBER *(Include area code)*
+44 (0)1895 616021

Final Report
Grant no. FA8655-09-1-3014

Hypersonic Transition Experiments in 3D Cone Flow with New Measurement Technique

Dirk Heitmann
Rolf Radespiel

Institut Für Strömungsmechanik
Technische Universität Braunschweig

March, 2012

Submitted to the European Office of Aerospace Research and Development

Contents

List of Figures

List of Tables

Summary

This is the final report on the project with grant number FA8655-09-1-3014 dealing with laminar-turbulent transition measurements on an inclined cone at hypersonic Mach number. The report summarizes the main results reported in the last reports. Furthermore the work conducted within the last period of six months is described.

Within the flow field of an inclined cone three different boundary layer instabilities appear: first and second mode instability waves and crossflow vortices. Two different measurement techniques were applied for investigating them: (i) IR-thermography was used for measuring stationary crossflow vortices. This instability was quantitatively measured. The position where these vortices evolve, their amplification and their wavenumber were determined. Furthermore experiments were conducted aiming on affecting this wavenumber by placing small roughness elements on the cone surface that generate vortices. (ii) surface mounted pressure sensors were used for measuring travelling instabilities. The second mode waves are characterized regarding the position on the model where they appear, their frequency content and their spatial extensions and wave structure. Also low frequency waves ($f \approx$ 20-40 kHz) were detected. These waves are so far interpreted as first mode waves, but since no stability computations are available this is uncertain. Also travelling crossflow vortices might cause this signal.

The measurements of the wave structure and the spatial extent of second mode wave packets required an uncommon cone model. In total tree different model were used within this project. The last report covered the design of a new model with extended possibilities for mounting sensors. In the meantime new measurements have been conducted with this model and they are reported here. Measurements with suited positioning of pressure gauges and correlations of their signals allowed measurements of the spatial extent and propagation direction of second mode instability waves. Furthermore, the new experimental results indicate the presence of low frequency waves and by analysis of the acquired data with higher order spectra new insights into the nonlinear stage of the transition process could be obtained.

1 Introduction

One major uncertainty in the aerodynamic design of high-speed vehicles results from laminar-turbulent boundary layer (BL) transition. This transition severely affects heat loads and drag. Increases in the heat flux by a factor of 3-8 are reported in the literature; see e.g. Schneider (2004). Despite of many efforts over the last decades the mechanisms leading to transition in high-speed boundary layers are still poorly understood. Experiments are typically conducted on simple generic models such as slender cones. Such a cone at zero angle of attack (AOA) generates a 2D flow field, where according to Mack (1984) two instability modes are amplified; the first mode (or Tollmien-Schlichting wave) and the second mode. The first mode is of vortical nature and at hypersonic Mach number only weakly amplified compared to the second mode. The second mode is considered as acoustic wave that is trapped between model and a critical layer inside the BL. Due to the recently found eligibility of surface mounted sensors progress was made in the investigation of the second mode, especially in “simple” 2D flow fields. For more complex 3D flow fields two further instability mechanisms become important: First, the Gortler instability, that appears on concave walls. There, counter-rotating vortices develop as consequence of the destabilizing effect of the centrifugal force as a certain boundary layer edge velocity is exceeded. Second, the crossflow instability, that appears in regions with lateral pressure gradient on curved surfaces. Outside the boundary layer the centrifugal forces and the pressure gradient are balanced and the streamlines are bent. Inside the BL the velocity decreases causing an imbalance of these two forces. Due to this imbalance a secondary flow in form of co-rotating vortices develops. Such instability e.g. appears on swept wings.

In this report measurements on an inclined cone are presented, where this crossflow instability also develops. Furthermore, due to the asymmetric shock the boundary layer edge velocity differs significantly depending on the position on the model. Therefore also first mode waves might be important in the transition process beside the second mode instability.

A 7deg half-angle cone was mounted with an AOA of 6deg to generate a flow field, where first and second mode waves develop, and where also the crossflow instability is present. Two different measurement techniques were applied. Surface covering measurements were conducted with a high-speed infrared camera. From these surface temperature data the heat flux normal to the wall was evaluated and the footprints of steady crossflow vortices appear in these images, thus enabling a quantitative measure of this instability. The frame rate does not allow for detecting convecting crossflow vortices. Time-resolved data are acquired from surface mounted pressure sensors, which allow the measurement of first and second mode instability waves. The experiments were conducted with different cone models. One of them is of an unusual design and offers extended possibilities for mounting the gauges. It is furthermore possible to rotate cone segments, thus allowing lateral sensor offsets. With this construction and suited evaluation procedures the extent of wave packets and the orientation of wave fronts could be determined.

In the last reports measurements of steady crossflow vortices were shown. These vortices were characterized regarding their position and their wavenumber. Also area-covering amplification rates were determined. Furthermore numerical computations of the mean flow were conducted. By comparing computed with measured heating rates the base flow computation could be checked, thus the simulations enable stability computations that are conducted at the moment. Beside this instability the second mode wave was measured. So far the second mode waves were characterized regarding the position where they occur and regarding their frequency content.

Since the last report two test campaigns were conducted. In the first campaign the focus was laid on unsteady fluctuations. From these measurements correlations between different sensors were obtained allowing statements about wave propagation and spatial extent of second mode waves. Furthermore disturbance spectra are given and bicoherence spectra provide some data about the nonlinear stage of the transition process. In the second test campaign roughness elements were placed on the cone in an attempt to influence the steady crossflow vortices. Thereby some roughness properties were varied such as thickness, diameter and spacing and the elements were placed at various positions on the cone model. Results for the cone with such elements are compared to results for the smooth cone.

2 Experimental Setup

2.1 Wind Tunnel

The experiments were performed in the Hypersonic Ludwieg Tube Braunschweig (HLB). The facility is described in detail in Estorf *et al.* (2004). A schematic of the facility is given in Fig. 1. The HLB is a wind tunnel that runs at a nominal Mach number $M_\infty = 6$, in a unit Reynolds number range of $[3 - 20] \times 10^6\ \mathrm{m}^{-1}$ for about 80 ms at conventional noise level. The noise level by means of pitot pressure fluctuations is according to Heitmann *et al.* (2008) between 1-1.6% depending on the initial driver tube pressure and on the position in the test section. The driver tube of the HLB is separated from the low pressure section, consisting of nozzle, test section, diffuser and a dump tank, by a fast-acting valve. The driver tube is heated along the first 3m upstream of the valve, accommodating the amount of gas that is released during one run. The valve consists of a streamlined center body on the tube's axis. The nozzle maintains an opening half angle of 3deg which results in slightly expanding flow in the test section with Mach numbers between 5.8 and 5.95 depending on the axial position and on the unit Reynolds number. The driver tube pressure is recorded with an accuracy of ±1%. The temperature in the driver-tube is measured at two positions during the run. It must be noted that the measured temperature difference between the upper and lower measurement positions can be as high as 30K due to temperature stratification. Hence, the measured value is not exactly the total temperature at the height of the model in the test section. Thus the determination of the unit Reynolds number is affected by uncertainties in total temperature, pressure and Mach number in the test section and the overall uncertainty is according to Estorf (2008) about ±2% in the relevant unit Reynolds number range. Typical flow conditions for the experiments reported are given in table 1. These are the flow conditions for the new experiments reported here for the first time. In this report also some results are shown that were already reported earlier, Kroonenberg & Radespiel (2009, 2010a, 2010b) Fischer & Radespiel (2011a, 2011b). For these results the flow conditions are given in the figures.

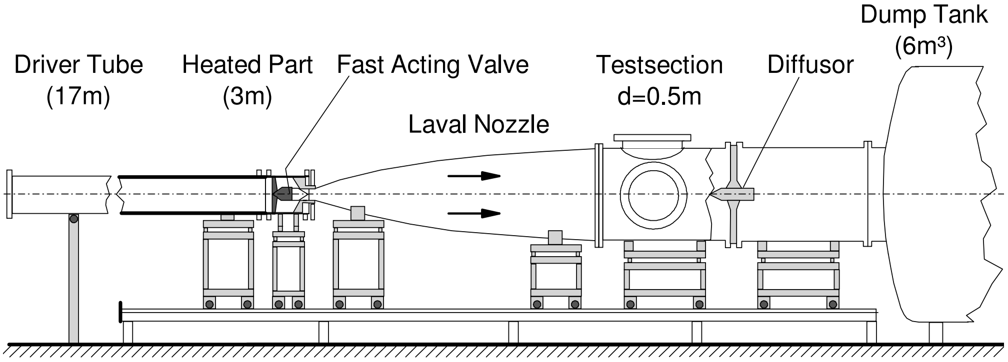

Figure 1: Schematic view of Hypersonic Ludwieg Tube Braunschweig (HLB)

Table 1: Flow conditions

p_0, kPa	T_0, K	Re_∞, 10^6 m^{-1}
600	476.6	5.03
800	471.7	6.81
1000	476.6	8.38
1200	471.5	10.2
1400	467.9	12.07

2.2 Instrumentation

An IR camera of type Phoenix DAS (company Indigo) was used. This camera has an InSb sensor that is sensitive in the mid IR range between 3-5µm wavelength. The resolution is 320×256 pixel and the maximum frame rate is 320Hz. An integration time T_{int} of 3-3.5ms is necessary for a reasonable signal-to-noise ratio resulting in lower frame rate. In most experiments T_{int} was set to 3.4ms resulting in a frame rate of 140Hz. I.e. that approximately 10 images were taken during steady wind tunnel flow. An objective with 25mm focal length was used.

Pressure fluctuation measurements were performed with PCB M131A32 sensors. In the last years these sensors were widely used for measurements of hypersonic instabilities. The sensors were flush mounted to the surface. The diameter of the gauges is 3.18mm. The active area is of rectangular shape (0.762×0.762mm²). Power was supplied by two PCB instruments (M482A22 and M483A), which, at the same time, performed signal conditioning. The sensors have sensitivities in the range of 0.02mV/Pa and a resolution of 7Pa. For further details the reader is referred to the manufacturer PCB Piezotronics (2009).

The pressure data were sampled with a Spectrum M2i.4652 transient recorder. The sampling frequency was set to 3MHz and the data was stored in 16 bit format. Time traces of 265ms length were recorded, consisting of about 180ms before/after and 80ms of data during the tunnel run.

2.3 Cone Model

Different cone models were used for the experiments. First measurements (reported in Kroonenberg & Radespiel (2009, 2010a, 2010b) were conducted with the model depicted in Fig. 2. It is a 7° nominally sharp cone made from Plexiglas to allow for IR measurements. Six pressure gauges were installed along one cone generator. Since the model was installed with an angle of attack the sensors could not in general be placed along a single streamline. Hence the development of individual second mode wave packets could not be measured and therefore a new model was designed.

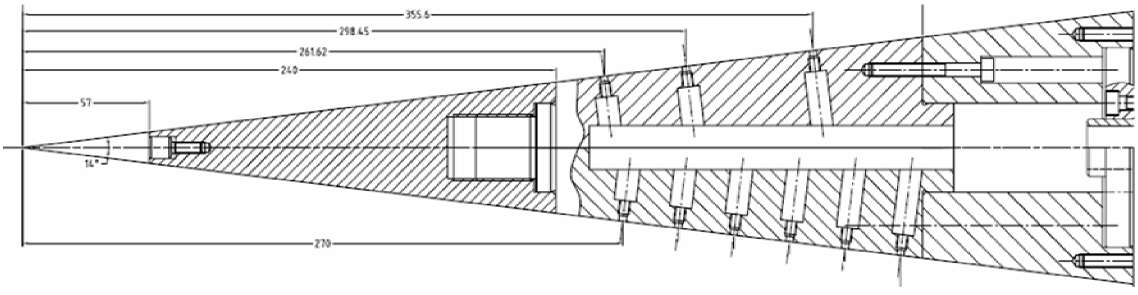

Figure 2: First cone model

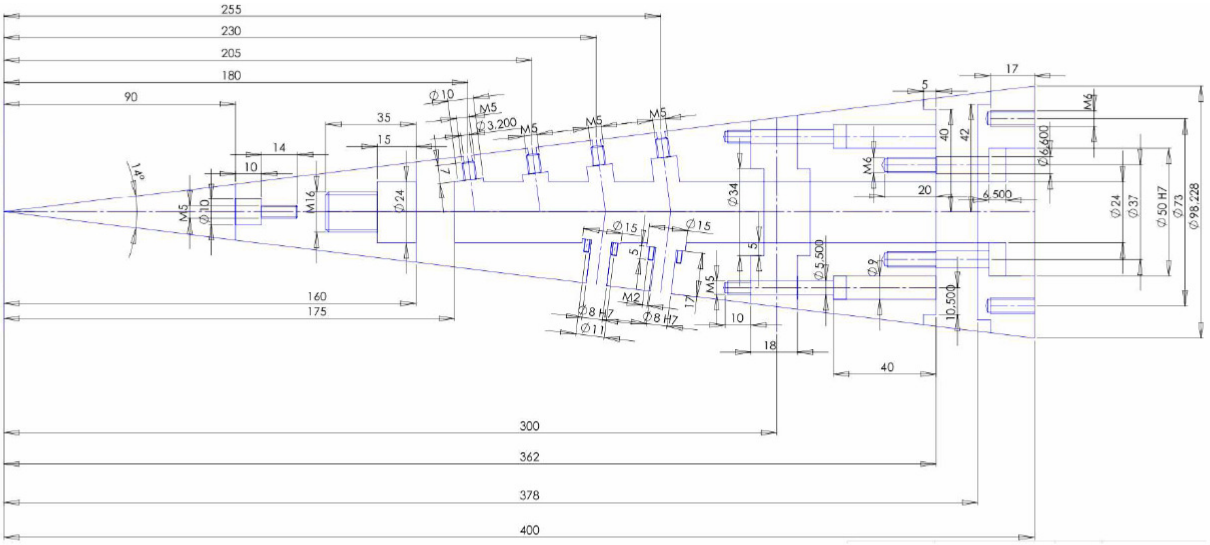

Figure 3: Second cone model

This new model is depicted in Fig. 3 and it consists of several Plexiglas parts, two of them being rotatable disks. The intention of this design was to successively rotate these disks until sensor signals correlate and individual second mode wave packets can be detected on at least two sensors. Unfortunately first tests with this cone model unveiled a lack of stiffness. During wind tunnel operation the alignment of the cone parts suffered resulting in steps and surface inhomogeneities.

Therefore another 7deg half-angle cone model was designed and built for the latest measurements. The design is based on experience from the second cone model and reported in Fischer & Radespiel (2011b). The outer surface of most of the cone is made from Plexiglas (black 811-Röhm-GS) to allow for infrared measurements. Temperature-dependent thermophysical properties of this material are given in Wolf *et al.* (2007). The model was coated (approx. 50µm) with Nextel Velvet Coating 811-21 which has an emissivity of about 97% within the measured spectrum. The model has a total length of 400mm and consists of 11 parts, some of them being rotatable disks for extended sensor positioning. These parts are put on a common shaft made from stainless steel, that guarantees for sufficient stiffness. The steel parts also make narrow fittings possible, which are necessary to avoid steps and imperfections at the connecting points as the disks are rotated. The model has a nominal sharp tip made from stainless steel. Its bluntness is estimated to about 100µm. The model is depicted in Fig. 4.

The model allows for the mounting of 10 sensors. Some sensors were placed as closely as possible together for correlation measurements. Also some sensors with lateral offset are available. This is to simplify these correlation measurements. Table 2 summarizes the measurement positions.

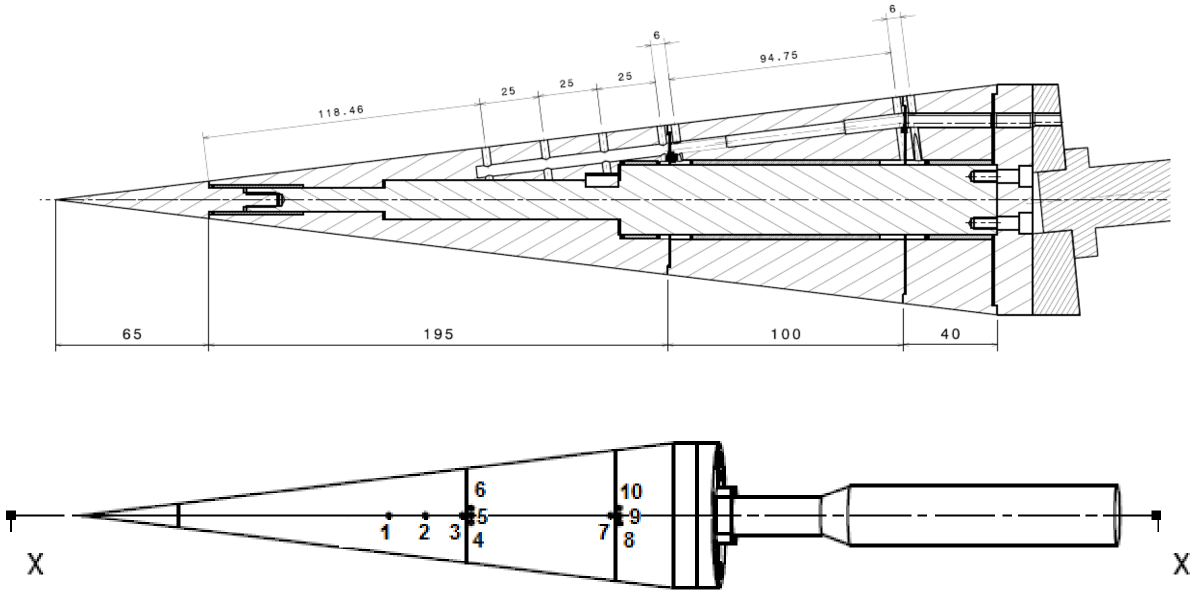

Figure 4: Third cone model

Table 2: Measurement positions for PCB pressure sensors

Sensor #	Axial distance from tip X, mm	Lateral offset dU, mm
1	207.5	0
2	232	0
3	257	0
4	263	-5
5	263	0
6	263	5
7	357	0
8	363	-5
9	363	0
10	363	5

3 Data Analysis

3.1 IR-Data

Prior to measurements the non-uniformity of the pixel-sensitivities was corrected first order accurate by a two point-calibration. Image coordinates were mapped to spatial coordinates by applying a conical 2D-grid to the cone surface. Furthermore, a temperature calibration was necessary to transform grayscale values into temperature. Therefore a black radiator was installed in place of the model and the calibration function was computed by a quadratic fit of the calibration points. Details on the temperature calibration including the emissivity correction and details on the spatial mapping algorithm are described by Estorf (2006).

An image based method for transient surface normal heat flux calculation from thermographic data was used (developed by Estorf (2006)). 1D nonlinear heat conduction was assumed for the calculation of surface heat fluxes from the transient temperature data. The heat conduction equation was solved numerically using finite differences. The unknown heat flux was found by the iterative regularization method: The surface temperature calculated from an iteratively improved heat flux is compared to the measured values in a least squares formulation. The gradient for iterative correction of the heat flux is found by solving the adjoint problem. The stopping criterion is adjusted to the noise level of the measured temperature data. The whole procedure including spatial and temperature calibration, non-uniformity correction and heat flux computation is described in detail by Estorf (2006, 2008).

During one tunnel 8-11 images were taken and the just mentioned procedure was performed. Then the average was taken to reduce noise.

In some figures the dimensionless heat transfer is used which is defined as the Stanton number *St*

$$St = \frac{\dot{q}}{\rho_\infty U_\infty (T_t - T_M) c_p}$$

with the surface heat flux $\dot{q}$, the specific heat of air c_p = 1005 J(kg K)$^{-1}$, the free-stream density ρ_∞, the free-stream velocity U_∞, the mean total temperature T_t and the model surface temperature T_M.

3.2 Pressure Data

Within this report power spectra of the pressure data were calculated to determine the frequencies of possible disturbances. The spectral density of the pressure signal was calculated by the discrete Fourier transform of the signal Φ that was multiplied by the Hann-window function *w(k)*. The discrete Fourier transform (DFT) of signal Φ is described as

$$\tilde{\Phi}_n = \sum\nolimits_{k=0}^{N-1} \Phi_k \cdot w(k)\, e^{-i2\pi nk/N} ,$$

with the number of data points N, the index of the signal $k = 0, \ldots, N-1$, the index of the Fourier series n and the Hann-window function $w(k)$

$$w(k) = \frac{1}{2}\left[1 - \cos\left(\frac{2\pi k}{N-1}\right)\right] \quad \text{for} \quad 0 \le k \le N .$$

The power spectrum of Φ as function of the frequency f is defined as the DFT of the auto-covariance function of Φ which is the second power of the DFT of Φ

$$PS_\Phi(f) = \pi \cdot \frac{f}{n} \cdot \left|\Phi(f)\right|^2 .$$

The power spectra were smoothed by a central moving average to reduce the noise at high frequencies. For every data point i, the spectral density was averaged over a range of data points, using both “past” and “future” data. The size of this range for point i corresponded to 0.01% of the frequency f_i. This means that the higher the frequency, the more data points were used to calculate the averaged spectral density.

For the latest test campaign the parameters for computing disturbance spectra were slightly changed. Therefore time traces of 60ms length were divided into segments of 1024 data points with an overlap of 768 data points. These windows were multiplied with a normalized Blackman window and Fourier transformed. Finally the average of the spectra was taken and a spectrum prior to the run was subtracted to reduce noise of the measurement chain. The obtained frequency resolution is $\Delta f \approx 2.9$kHz.

Furthermore a plot of the bicoherence will be shown to assess nonlinear effects and interactions as the instability waves break down. For an effective energy transfer between disturbance modes a constant phase angle between the oscillations at the different frequencies f_1, f_2 and f_3 is necessary. A bispectrum tests the signal on this property and it is defined as

$$B(f_1, f_2) = S(f_1) \cdot S(f_2) \cdot S^*(f_3) ,$$

where S denotes the complex spectrum and S^* the complex conjugate spectrum. If waves are present at the frequencies f_1, f_2 and $f_3 = f_1 + f_2$ and if there is a constant phase lag between these waves $B(f_1, f_2)$ is not zero after the averaging over many windows has been conducted. The bispectrum is amplitude dependent. Therefore it is typically normalized to values between 0…1. Then it is called bicoherencespectrum.

$$bi^2(f_1, f_2) = \frac{|B(f_1, f_2)|^2}{S(f_1) \cdot S(f_2) \cdot S(f_3)}$$

The bi^2-value can be interpreted as fraction of the energy at frequency f_1+f_2 that is due to nonlinear effects.

4 Results and Discussion

At first results for the smooth cone are presented. Thereby we start with IR measurements which show the surface footprints of the steady crossflow vortices. Special attention is laid on repeatability and also some results of numerical computations (partially by G. Candler, University of Minnesota) are shown.

Then results obtained with the surface mounted high-frequency pressure sensors are shown. These measurements reveal the presence of second mode instability waves. In addition low frequency waves were detected. The latter waves are so far interpreted as first mode waves. While the second mode instability is characterized concerning the locations, where they appear, their frequency content, their spatial extent and their wave orientation, the first mode instability could only be detected. Due to the comparatively small amplification further analysis was not possible.

The last section covers results about an attempt to modify the wavenumber of the steady crossflow vortices. Therefore different types of roughness elements were applied to the cone surface and it is shown that the wavelength can indeed be modified. However, a transition delay was not possible due to the necessity to mount the roughness elements very close to the tip. There the boundary layer is very thin and thus additional disturbances were introduced.

4.1 Steady Instabilities for the Smooth Cone

Figure 5 shows composite images of the calculated heat flux on the cone. The flow conditions for each shown run are given in the caption. On the cone several longitudinal structures are visible which are interpreted as the footprints of crossflow vortices. For all runs the flow was partially turbulent which is indicated by the areas with high values of the heat flux (green and red areas). It is interesting to observe the difference in the shape of the assumed transition front between the areas with smaller (Θ<80deg) and larger circumferential angles. For smaller angles an almost straight transition line is found while at larger angles a zig-zag-pattern was observed that is typical for crossflow transition.

The images are composed of two different tunnel runs, where the camera was placed aside or on the leeward side of the cone. For all four figures these two camera views give very similar results in the overlap-region. This can already be interpreted as indication of reasonable repeatability. The repeatability was further tested by performing several tunnel runs at exactly the same flow conditions. These results are depicted in Fig. 6. For three different flow conditions (given in the caption) in total five tunnel runs are shown. In all figures the crossflow vortices appear similar and hence the repeatability justifies further evaluation. Note that some further information about repeatability was given in an earlier report (Kroonenberg & Radespiel (2009)).

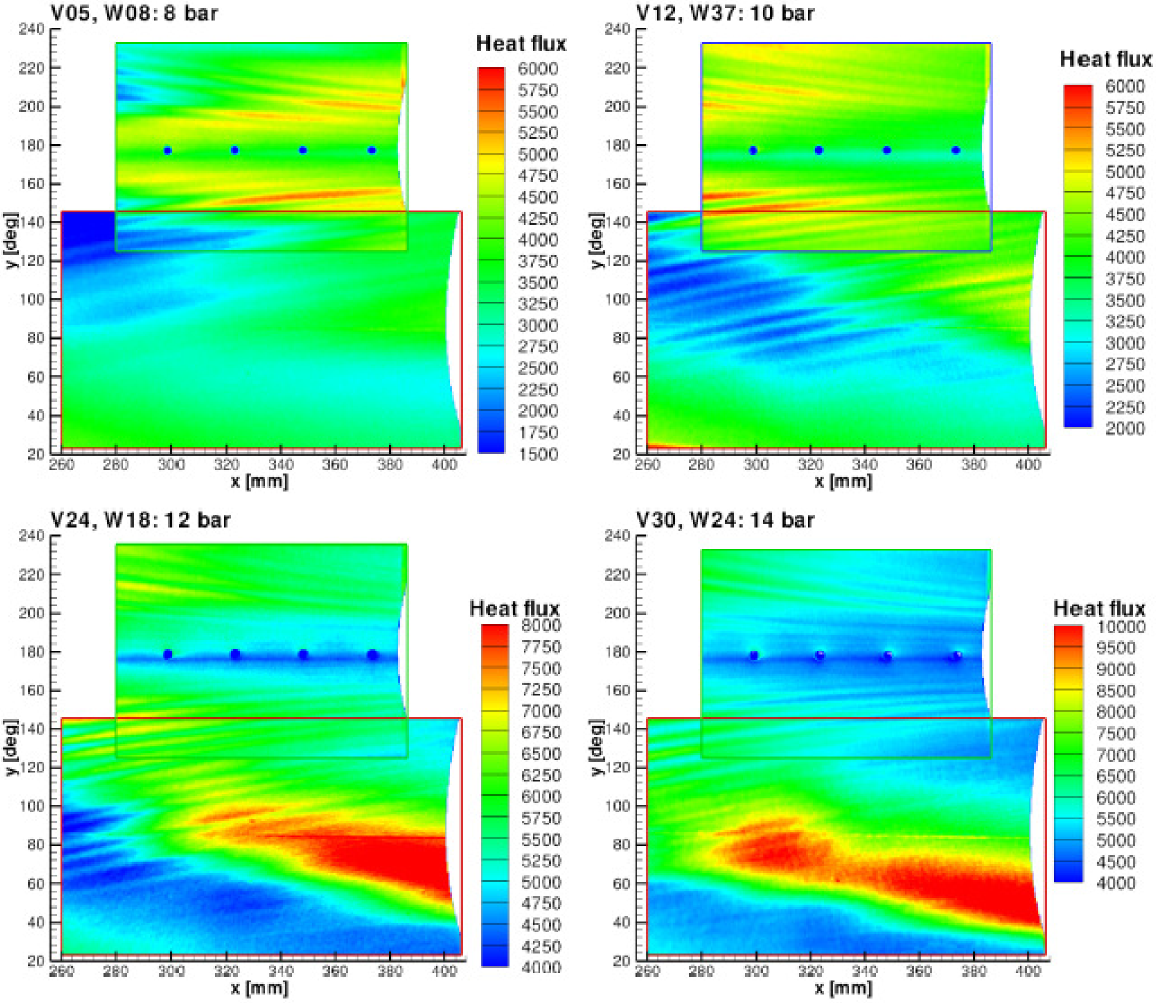

Figure 5: Composed infrared images (top and side view) for different initial pressures. The color represents the calculated heat flux in W m^{-2} on the cone surface. The x-axis shows the distance from the tip of the cone in mm. The y-axis shows the circumferential angle Θ in degree. Top left: p_0 =8 bar, top right: p_0 =10 bar, bottom left: p_0 =12 bar, bottom right: p_0 =14 bar.

Figure 6 was just given as measure of repeatability, but it includes also further information. Since the vortices might have their origin in very small surface inhomogeneities the cone model was rotated in 45deg steps. Therefore any inhomogeneities are at different locations in the figures and indeed a weak influence is present. However the effect is almost negligible since the surface was carefully grinded.

In the most recent measurements the camera was placed aside, since there the vortices appeared most clearly. The pressure sensors were facing sideward since previous measurements indicated maximum second mode amplitude there. So far the cone was not unrolled to spatial coordinates. Instead always the circumferential angle Θ was used. To obtain “fully” spatial coordinates also the y-axis is transformed in the following figures. In Fig. 7 the y-axis is defined as the cone radius at the specific x-location times the circumferential angle Θ in radians.

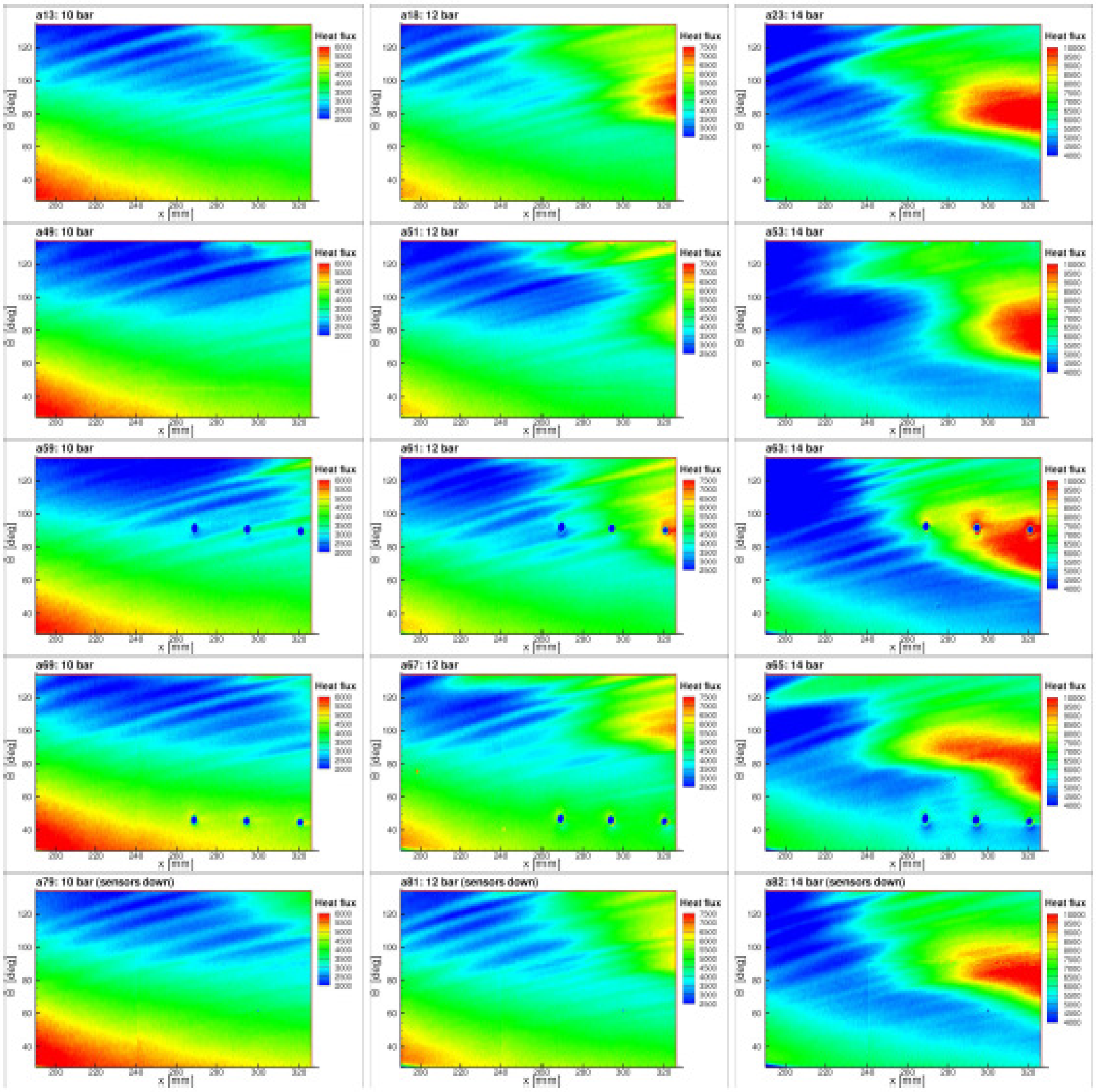

Figure 6: Heat flux images for different sensor positions. The upper images are made with a sensor position of 180◦ (facing upward). The cone was rotated with 45◦ steps, the lowest images were made with a sensor position of 0◦ (facing downwards). Left column: measurements at p_0 = 10 bar, middle column: measurements at p_0 = 12 bar an right column: measurements at p_0 = 14 bar.

Figure 7 depicts the measured heat flux on the unrolled cone for three flow conditions. Beside the camera field of view also the cone is indicated. At the lowest Reynolds number the flow is entirely laminar. There is moderate heating on the windward side but no transition induced heat flux-increase. In subfigure (b) the crossflow vortices are clearly visible in the upper part of the model. In the lower part ($X^* >=$ 300mm; $r\,\theta \approx$ -20mm) there is an increase in heat flux indicating transition. This increase is rather smooth and the transition seems to be initiated from first or second mode waves in contrast to the transition in the upper part of the figure ($X^* >=$ 260mm; $r\,\theta \approx$ 20mm).

In the case of the highest Reynolds number the transition position moves forward. The upper part is again crossflow dominated and the lower part exhibits a smooth shape indicating a first or second mode dominated scenario. Note that the results of Fig. 7 were obtained with cone model 3 (Fig. 4) and the results of Figs. 5 and 6 with cone model 1 (Fig. 2). The similarity of the results shows that despite of the more complex design no surface roughness is present as the flow field seems to be undisturbed.

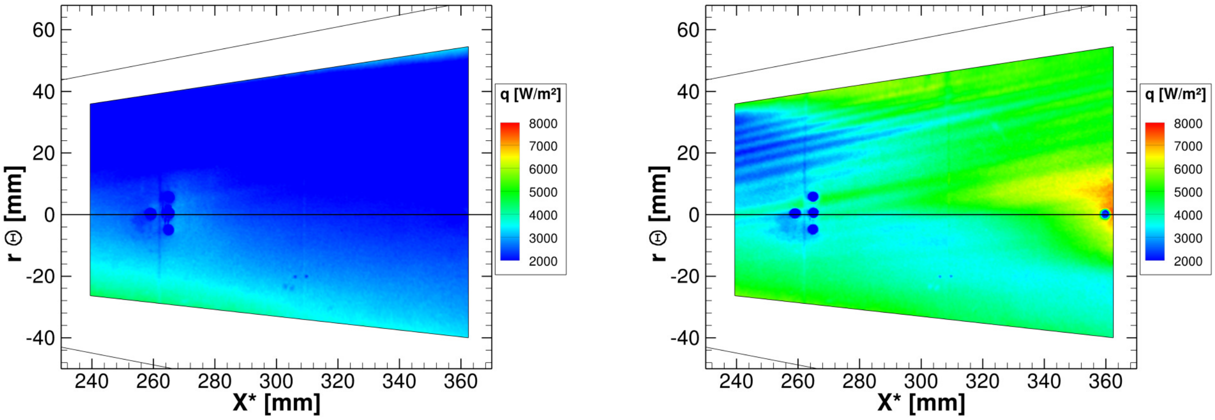

(a) $p_0 = 600$ kPa, $T_0 = 476.6$ K
$Re_\infty = 5.0 \times 10^6$ m^{-1}

(b) $p_0 = 1000$ kPa, $T_0 = 476.6$ K
$Re_\infty = 8.4 \times 10^6$ m^{-1}

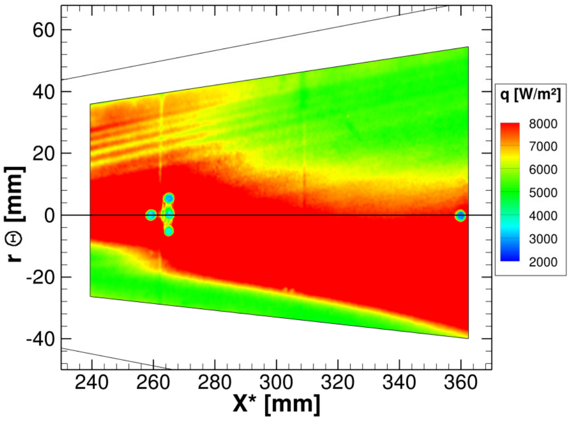

(c) $p_0 = 1400$ kPa, $T_0 = 476.9$ K
$Re_\infty = 12.1 \times 10^6$ m^{-1}

Figure 7: From IR-data computed heat fluxes normal to the wall for different flow conditions on the unrolled cone, the x-axis X* displays the surface distance, the y-axis is defined as radius times circumferential angle θ in radians

The IR-data can be used to determine area covering amplification rates. Two slightly different calculation procedures and some exemplarily results were given in Kroonenberg & Radespiel (2010a). Both procedures yielded too low *N*-factors due to the applied averaging over at least some camera pixels. The method that yielded more realistic results is summarized here briefly. The calculation takes place in four steps:

1. Calculation of the heat flux (Fig. 8a),
2. Application of a high-pass filter to remove the mean-flow heat-flux variation while retaining the crossflow amplitudes (Fig. 8b). Hence the variations with a low frequency, corresponding to spatial periods less then about $\Theta = 20°$ in circumferential direction are filtered out,
3. The amplitude of the filtered heat-flux is calculated assuming a sine wave-form of the data (Fig. 8c). The assumption that the crossflow vortices approximate a sine-function was used to develop two methods to estimate the amplitude of the filtered heat flux. The following procedure proved to be more reliable. For information about the other tests the reader is referred to Kroonenberg & Radespiel (2010a).

   The standard deviation σ is calculated for every position on the cone over an area of 9.1mm × 11.0°. Then the amplitude of the assumed sine-function is calculated:

$$A_i = \sqrt{2} \cdot \sigma .$$

4. The relative *N*-factors are calculated (Fig. 8d) according to,

$$\Delta N_i = \ln\left(\frac{A_i}{A_0}\right),$$

where A_i is the amplitude at position *i* on the cone and A_0 the initial amplitude. The value of A_0 is chosen as the most upstream value on the infrared image of the cone by following the crossflow footprint (for this example on the x = 184 mm or the Θ = 43° axis).

The alternative last step is to calculate the spatial crossflow amplification rates $-\alpha_i$ (Fig. 8e),

$$-\alpha_i = \ln\left(\frac{A_{[i+\Delta x]}}{A_i}\right)\cdot \Delta x^{-1},$$

where Δx represents the distance over the cone surface between location *i* and $i+\Delta x$ which both are in line with the crossflow vortices (for this example $\Delta x \approx 20$ mm).

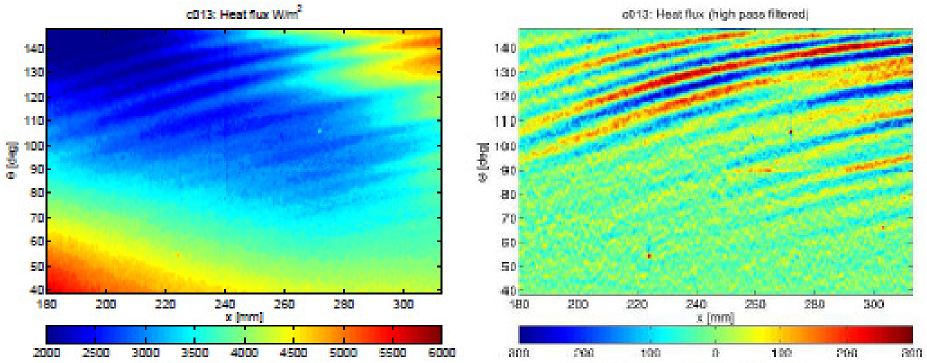

(a) Heat flux (W m^{-2})

(b) High-pass filtered heat flux

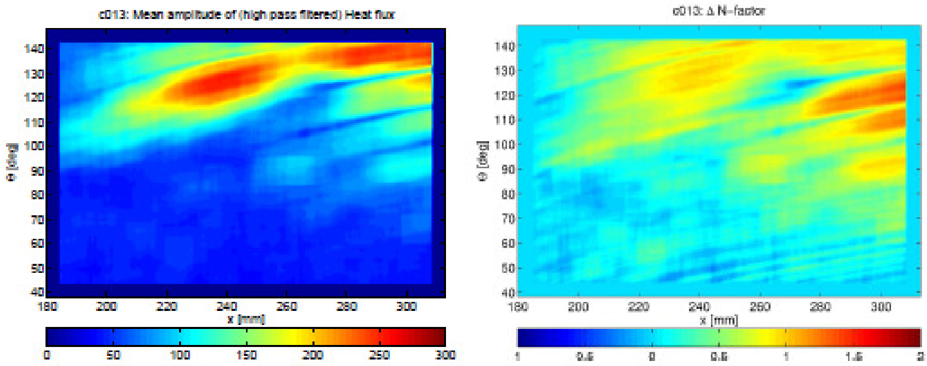

(c) Amplitude of the filtered heat flux

(d) The calculated relative N-factor ΔN

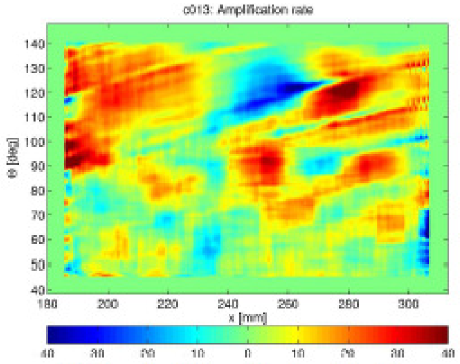

(e) The calculated amplification rate $-\alpha$

Figure 8: Computation of relative N-factors. Run at p_0 = 10bar, $Re_\infty = 8.54 \times 10^6$ m^{-1}. The x-axis shows the distance from the tip in mm. The y-axis shows the circumferential angle Θ.

The most crucial step is the calculation of the area-covering amplitude (step no. 3). The method is restricted to calculate averaged amplitudes, which are always smaller than the actual amplitudes, see Kroonenberg & Radespiel (2010a) for more details. It seems that the assumption of a sine wave is not in any case appropriate. Hence the determination of area covering amplification rates or *N*-factors includes some uncertainties and is restricted to only small areas.

The measured heating rates can be compared to numerical computations, see Fischer & Radespiel (2011b). The laminar base flow for both the cone at zero angle of attack and for the inclined cone was computed using the DLR TAU code. All calculations were carried out in a steady-state mode with fully laminar simulation. The numerical mesh was generated with the program tool Gridgen. The grid was divided into 5 blocks with a total cell number of 7,182,427. The topology is shown in Fig. 9. The sharp nose is approximated by a radius of 4.2 µm and meshed by a block of unstructured tetraedra cells (Fig. 10). The farfield is structured by hexaeder cells. The clustering at the cone surface is 65 cells in circumferential and 650 cells in axial direction (cp. Fig. 9). The resolution of the boundary layer is about 60 points and will be shown later. To reduce the cell number a symmetry plane is defined in the xy-layer.

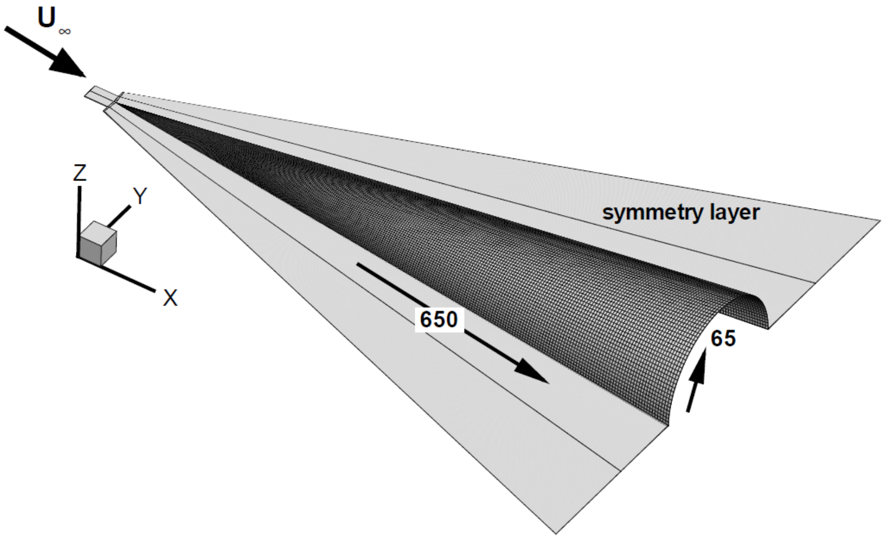

Figure 9: Topology of the numerical mesh

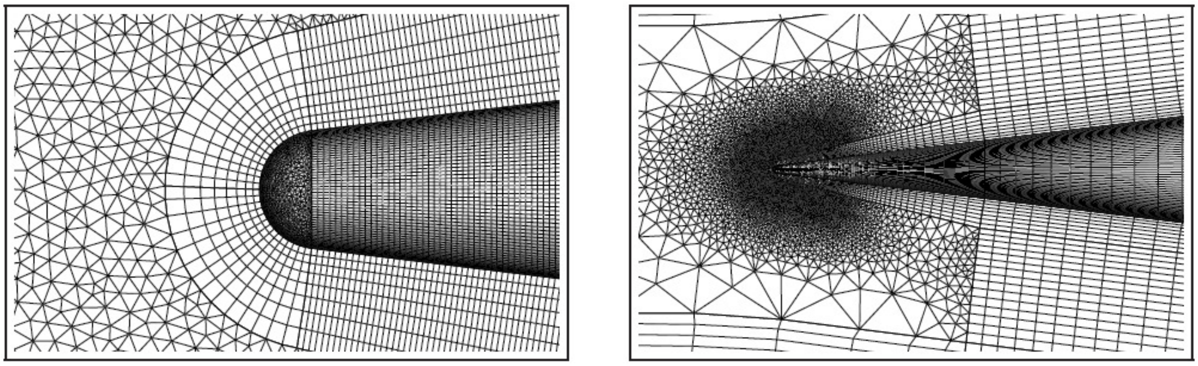

Figure 10: Topology of the numerical mesh close to the tip

For the cone at zero AOA analytical solutions for the boundary layer exist and these solutions can be used as validity check of the flow computation. Therefore the boundary layer edge conditions were computed according to the Taylor-Macoll equation; see e.g. Sims (1964). Based on this edge conditions the boundary layer was computed according to the procedure described by van Driest (1952). Since the similarity method computes flat plate flow another transformation (Mangler (1945)) is required to transform the results to conical flow.

The comparison between computed boundary layer profiles and the similarity solution is depicted in Fig. 11. The TAU solution is given by the symbols and for each cell one symbol is given. The amount of symbols shows that the boundary layer is properly resolved. Also the agreement between TAU computation and similarity solution is reasonable and this agreement is considered as validity check of the numerical simulation.

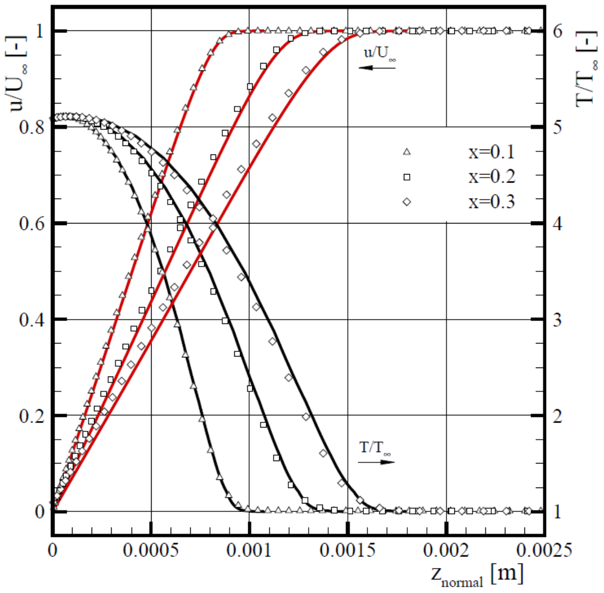

Figure 11: Boundary layer at different axial positions for the cone at zero AOA (CFD solution: symbols, similarity solution: lines)

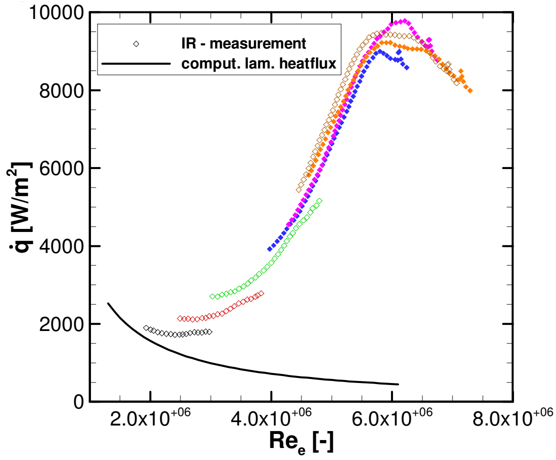

Figure 12: Heat flux on the cone at zero AOA. Computation for fully laminar flow. Experiments show transitional heat flux augmentation

Also the heat transfer can be extracted from the simulations and a comparison between computed and measured heat flux is given in Fig. 12. The computed heat flux was already given in an earlier report (Fischer & Radespiel (2011b)) and now experimental results are added. The computed heat flux decreases with increasing Reynolds number due to the growing boundary layer. The experiments show an increase in heat flux by a factor of 5 due to laminar-turbulent transition. However, in the laminar region the computed heat flux agrees to the experimental results.

Also by Graham Candler (University of Minnesota) some computations were conducted and these computations are compared to experiments in Fig. 13. Shown is the heat flux on the unrolled cone (x-Θ-plane) for one specific tunnel condition. More comparisons between computed and measured heat fluxes can be found in Kroonenberg & Radespiel (2010a). For the measurements the figure includes crossflow vortices, but the base flow is very similar in both cases. A more quantitative view is provided in Fig. 14. There a line is extracted from a contour plot similar to that of Fig. 13. The agreement between computed and measured heat flux is very good.

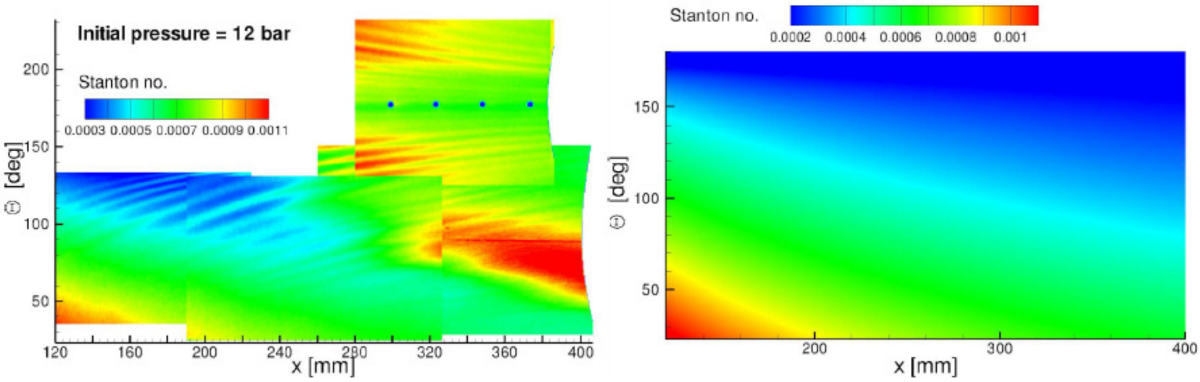

Figure 13: Comparison of computed and measured heat flux. Computation by G. Candler (University of Minnesota). Flow conditions: p_0 = 12bar, $Re_\infty = 9.5 \times 10^6 \mathrm{m}^{-1}$

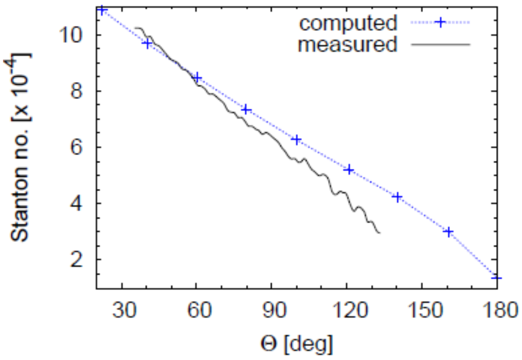

Figure 14: Cross-section of the heat transfer, flow conditions: p_0 = 10bar, $Re_\infty = 8.1 \times 10^6 \mathrm{m}^{-1}$

4.2 Unsteady Instabilities for the Smooth Cone

Additional to the infrared images, pressure data were gathered from high-frequency sensors that were flush to the cone surface. Spectral analysis of the time series showed if the flow was laminar, turbulent or if pressure fluctuations occur due to boundary-layer instabilities. To change the position of the sensors, the cone was rotated in steps of 45deg (sensors facing windward = 0° and facing leeward = 180°). The infrared images, which were taken with different sensor positions, confirmed that there was no measurable effect of the sensor roughness on crossflow vortices or transition front, cp. Fig. 6.

Figure 15 shows the calculated pressure power spectra for four selected wind tunnel runs with cone model 1. The figures on the left had the pressure sensors located at 90° and the figures on the right at 135°. Unfortunately, during the measurement campaign sensor no. 3 broke and is therefore not shown here. In both upper figures (runs at p_0 = 8 bar) a clear peak in almost all pressure signals is visible which indicates the occurrence of second-mode instabilities within the laminar flow. Figure 15 (lower panel) shows the spectra for two runs at an initial pressure of 10 bar. The left figure shows an example of the transition process: sensors 1 and 2 indicate a laminar flow, sensor 4 shows a peak in the spectrum which indicates second-mode instabilities, the last sensor no. 6 indicates turbulent flow. The right figure in the lower panel shows that the transition process at Θ = 135° occurs closer to the apex. The sensors 4–6 show already turbulent flow in this case.

Table 3 shows the frequencies of pressure fluctuations (as shown in Fig. 15) for several runs at different initial pressures. The frequency of the instabilities depends on the initial pressure and the position of the sensors on the cone. The higher the initial pressure (and the Reynolds number) the higher and broader the frequency range. For the lower values of p_0 the instabilities appear higher on the cone, i.e. at $\Theta \approx 135°$. The runs with higher values of p_0 show the instabilities at smaller Θ –values (45°) and the flow is already turbulent at the higher positions (90–135°). Table 3 also shows combinations of sensor position and initial pressures with no entry (indicated by '-'). For these cases two possibilities exist (i) the Reynolds number is too small to induce these unsteady boundary-layer instabilities, or (ii) the frequencies of the instabilities were too high and could not be resolved by the pressure sensors.

The results of the pressure sensors were confirmed by the corresponding infrared images (see e.g. Fig. 5). For example, the positions of the pressure sensors which showed turbulent spectra and the areas with high heat flux values corresponded well to each other.

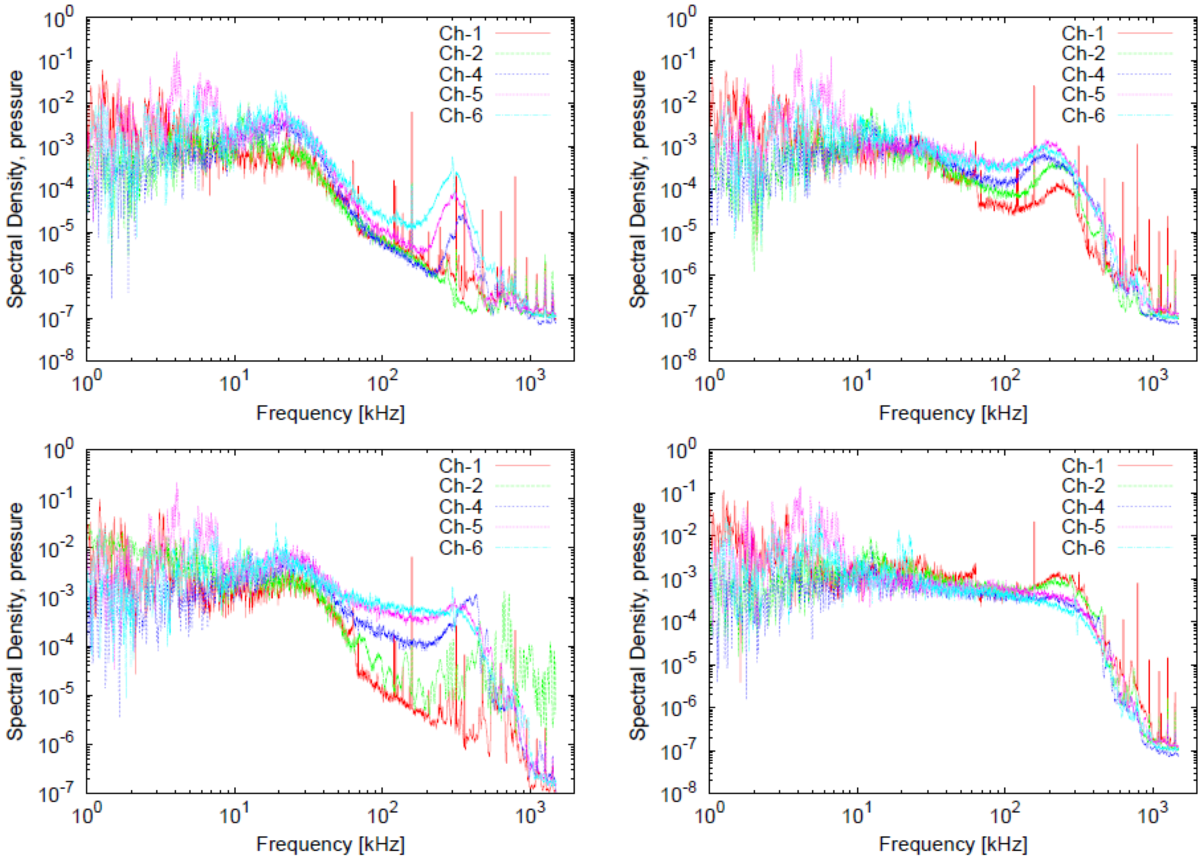

Figure 15: Power spectra of the pressure signals. All spectra are smoothed to reduce the noise in the higher frequency part. Upper left: p_0 = 8 bar with a sensors position of 90° (facing horizontally). Upper right: (p_0 = 8 bar) with a sensors position of 135°. Lower left: p_0 = 10 bar with a sensors position of 90° (facing horizontally). Lower right: p_0 = 10 bar with a sensors position of 135° (see also Table 3).

Table 3: Frequency of the boundary-layer instabilities for several initial pressures p_0 and sensor positions. The values in brackets are the corresponding sensor numbers (starting at 1 nearest to the tip of the cone).

p_0	sensor position			
[bar]	0° (windward)	45°	90°	135°
6.00	-	-	-	150-180 kHz (2-6)
8.00	-	-	300-350 kHz (4-6)	200-250 kHz (1-6)
10.00	-	440 kHz (6)	300-400 kHz (4-5)	250 kHz (1-2)
12.00	-	450-500 kHz (4-6)	500 kHz (1-2)	turbulent (1-6)
14.00	450 kHz (6)	turbulent 4-6	turbulent (1-6)	turbulent (1-6)

From the IR-data shown in the last section we conclude that the transition on the windward side is dominated by first or second mode instability waves and by the crossflow instability on the cone shoulder. On the shoulder (say $\Theta \approx 90° - 135°$) the second mode waves could be detected best. Therefore in the last measurement campaign, that aimed on investigating the wave structure, the sensors were placed aside at $\Theta = 90°$. These measurements were conducted with cone model 3 and the measurement positions were closer to the tip. In addition different parameters for the spectra-computation were chosen resulting in less noise due to more averaging.

Figure 16 shows disturbance spectra at the most forward position for different Reynolds numbers. For $p_0 = 6$ bar the flow is laminar. No significant signal is visible in the frequency range of the second mode (say $300 < f$, kHz < 500), but at about 30 kHz a small peak can be seen. With increasing Reynolds number a peak related to the second mode develops and the amplitude at low frequencies also increases. Unfortunately no calculations of the linear stability theory are available, but so far this peak is considered as indication of first mode instability. Note that this peak was also present in previous measurements (Fig. 15 top left image) although it was not as clear.

In Fig. 17 disturbance spectra for a single run at $Re_\infty = 10.2 \times 10^6$ m^{-1} are given with the new evaluation parameters. These are similar to the data of Fig. 15. The first sensor shows only very small amplitude for the second mode. This amplitude increases for the rear positions. At the two rearmost positions the flow seems to be turbulent. Also for the first mode wave growth seems to occur, but here it is not as clear as in Fig. 16. Between the foremost and the second sensor the amplitude seems to decrease. The reason for this is not clear. So far it is assumed that this effect is caused by the measurement equipment. The active area of the gauges has a rectangular shape and its orientation is unknown. This possibly affects the response of the gauges to travelling waves. However, in both figures two peaks appear which are related to the second mode and (probably) to the first mode instability.

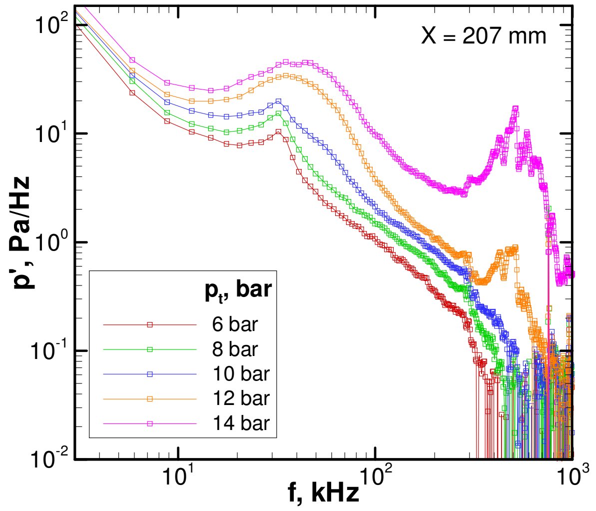

Figure 16: Disturbance spectra measured at X=207 mm for different Reynolds numbers

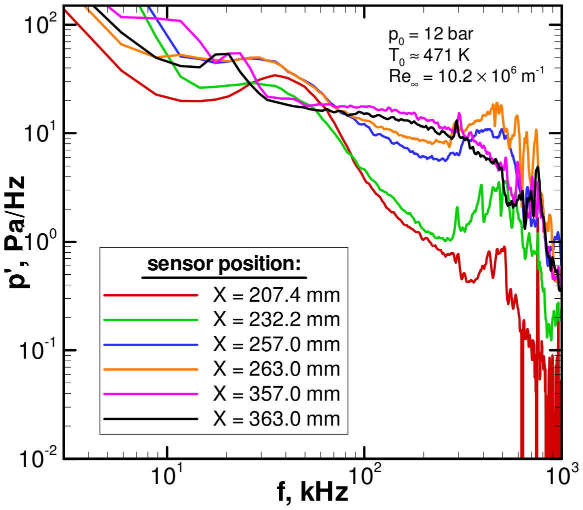

Figure 17: Disturbance spectra for different positions at $Re_\infty = 10.2 \times 10^6$ m^{-1}

The waves related to these peaks appear in the time traces as packets consisting of only a few oscillations. Due to their different history and their different amplification they appear random. A second mode wave packet is exemplarily depicted in Fig. 18. One can infer from its cycle period that it is a second mode wave and not a low frequency (probably TS) wave. Time traces of four sensors are shown, three of them being at the same axial distance to the apex. The first sensor shows a wave with approximately 50Pa amplitude. The subsequent sensor shows the amplification, but the exact amplitude can not instantaneously be specified since the wave possible passed the X=263mm position between the measurement positions $r\theta$ = 0mm and $r\theta$ = 5mm.

In the next measurements the cone segment accommodating the sensors at X=263mm was rotated in steps of 1mm and cross-correlations were computed. One of these correlations is depicted in Fig. 19. In this case the sensors had no lateral offset and the waves did not pass directly over the gauges. Hence the correlation is due to some spatial extent of the waves. The correlation exhibits a cycle period that allows interpreting them as second mode wave packet. However, the curve appears deformed and this is interpreted as consequence of the superposition with waves at different frequencies, i.e. frequencies in the range of 30 kHz; cp. Fig. 16.

For the inclined cone it is difficult to find waves on several sensors since the flow direction and the group velocities are also inclined. This inclination is not necessarily the same as the angle of attack. Therefore, the direction of the group velocity had to be identified by rotating one of the sensors and computing cross-correlations. Then the maximum correlation indicates the direction of the group velocity. Also the spatial extent of the "average" wave packet can be extracted from such measurements. This is depicted in Fig. 20.

The oblique direction of wave velocity was included in the analysis as the correlation at the rotated sensor with dU=1mm gave the largest correlation coefficient. Actually the result of a cross-correlation is the signal similarity as function of temporal offset. Here, the temporal offset was multiplied with the convection velocity. This is the surface distance between the two sensors divided by the time delay, at which the correlation is maximum. Hence we display a spatial distribution of pressure cross-correlation in a streamwise s-coordinate and a normal n-coordinate. The size of the "average" wave packet is about 8mm in streamwise coordinate and 3 mm in normal direction.

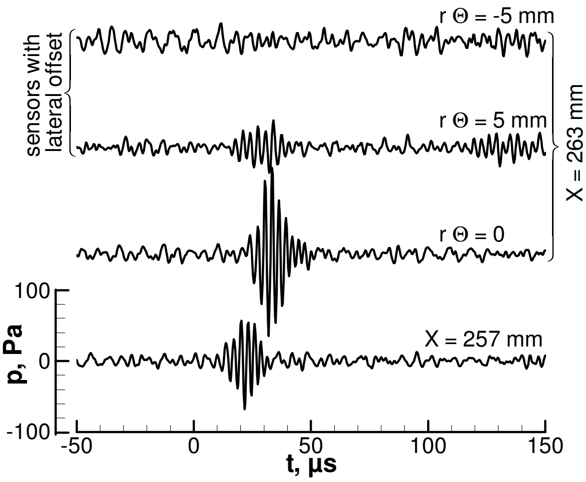

Figure 18: Time traces of four sensors (Bandpass-filtered between 100…600 kHz), p_0 = 800kPa, T_0 = 471.7 K, Re_∞ = 6.81× 10^6 m^{-1}

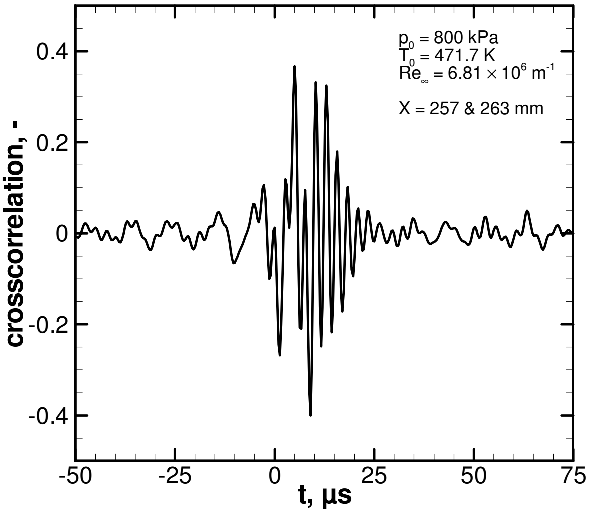

Figure 19: Example of a cross-correlation between sensors at X=257 & 263 mm, flow conditions like in Fig. 6, sensors had no lateral offset ($r\theta$=0mm)

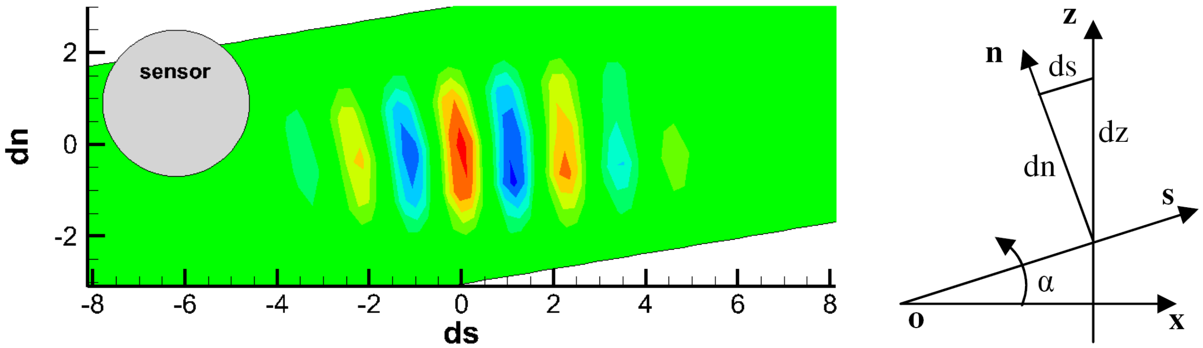

Figure 20: Contour plot of cross-correlation between sensors 7 & 9 (cp. Fig. 2) for different lateral offsets, axial distance is ≈6mm, flow conditions as in Fig. 6

The wave fronts are aligned normal to the streamwise direction as typical for second mode waves (see e.g. Mack (1984). We note that the size of the wave packages is smaller than for the non-inclined cone, see Heitmann *et al.* (2011) for comparison. This is mainly caused by the rapid changes of the boundary layer thickness as compared to axisymmetric flow. The tuning of the second mode wavelength to the BL thickness causes a different amplification behaviour. The wave packets rapidly change their wavelength and frequency content and do not grow as large as for the non-inclined cone. The sensors are quite large compared to the wavelength as indicated in the figure. But the active area of the gauges is smaller (0.762×0.762mm²) and about the same as half the wavelength. The measured amplitudes might be subject to some kind of wave averaging, but this would affect all sensors and hence the relative error is small.

Once the waves attain a certain critical amplitude nonlinear effects start to set in. Then the waves can no longer be considered independent and wave interactions take place. The presence of two unstable frequency regions makes a study of this phase appear interesting.

Since only surface measurements were conducted only there the signal can be analyzed. However, we note that the intensity of nonlinear effects changes over the height of the boundary layer, see e.g. Bountin *et al.* (2008). Very close to the wall the intensity decreases resulting in very small bi^2-values obtained from the surface pressure measurements. Such small bi^2-values are also reported by Fujii *et al.* (2011). Therefore the following image just gives an impression on which waves interact but not necessarily on the intensity of the nonlinear effects.

The bicoherence provides information about wave interactions between frequencies f_1, f_2 and $f_3 = f_1 + f_2$. However, it does not give information in which direction the nonlinear interaction takes place and additional data are necessary, e.g. in form of a disturbance spectrum. Both spectra are given in Fig. 21. In the spectrum (Fig. 21 (a)) the peak at $f \approx 300$kHz is related to the second mode. The increased bi^2-value for waves at $(f_1, f_2) \approx$ (300kHz, 300kHz) can indicate the generation of a harmonic and the spectrum in subfigure (a) indeed shows signal at approximately 600kHz. Also the first mode has become nonlinear and a harmonic is generated. This is difficult to see in subfigure (a) since the peak is rather broad, but at least a deviation to a standard distribution can be seen at $f \approx 40$kHz. Also interactions between first and second mode waves seem to occur as indicated by bi^2-value at $(f_1, f_2) \approx$ (250-350kHz, 20kHz).

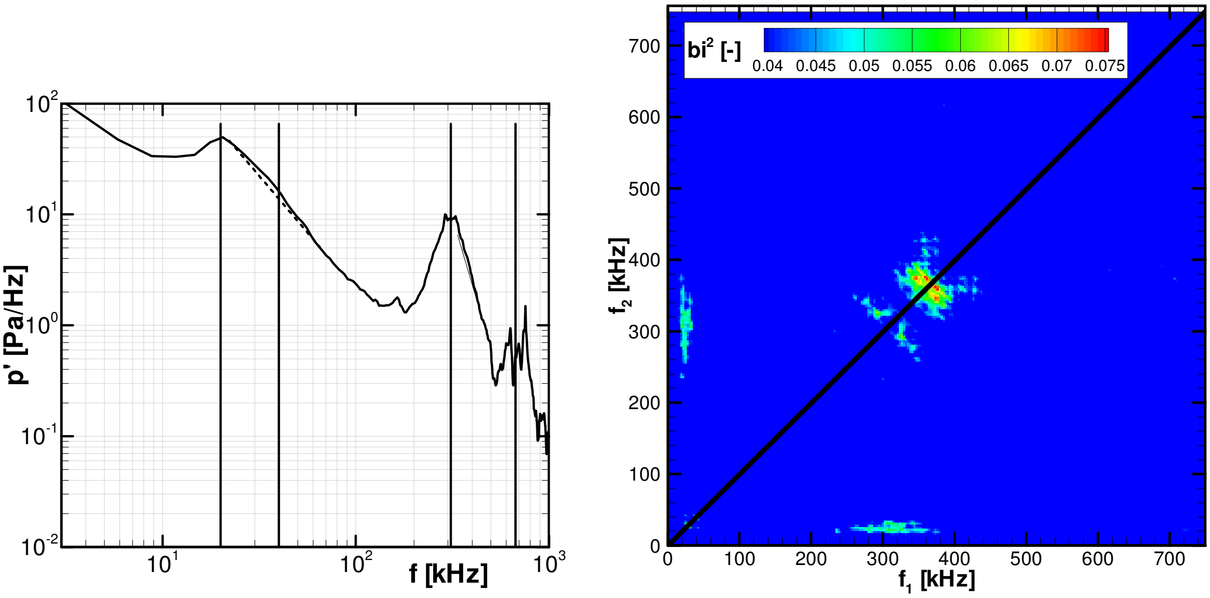

(a) disturbance spectrum

(b) bicoherence spectrum

Figure 21: Bicoherence spectrum and corresponding disturbance spectrum computed at X=363mm, flow conditions: p_0=800kPa, T_0=471.7K

4.3 Changing Properties of Crossflow Vortices

Already for the smooth cone crossflow vortices develop and the wavelength depends on the flow conditions as shown section 4.1 or in the previous reports on this project, see Kroonenberg & Radespiel (2009, 2010a, 2010b) and Fischer & Radespiel (2011a, 2011b). The measured wavelength can be compared to numerical data (published e.g. in Balakumar (2009)). Although the flow conditions and position on the cone model do not agree the unstable wavenumbers seem to be consistent. One example taken from Balakumar (2009) is given in Fig. 22 and compared to present measurements. Balakumar reports unstable wavenumbers *m* = 40-70, whereas the actual measurements show *m* = 45-60 depending on the position on the cone; cp. table in Fig. 22(b). Note, that Balakumar shows the crossflow vortices as contour of velocity fluctuations while in the present measurements the heat flux was measured. Of course the wavenumbers can nevertheless be compared.

The aim of the measurements presented here was to change this wavenumber *m* by placing roughness elements. Thereby values of *m* that are larger than for the smooth cone are of special interest, since it might be possible to delay transition in the crossflow dominated regions of the cone. Such a transition delay was e.g. shown by Saric *et al.* (1998) in experiments on a swept wing or more recently by Schuele (2011) in experiments on an inclined cone at Mach 3.5.

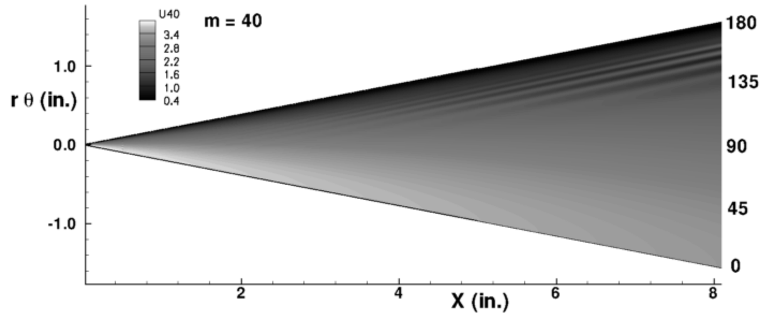

(a) numerical data (Balakumar (2009))

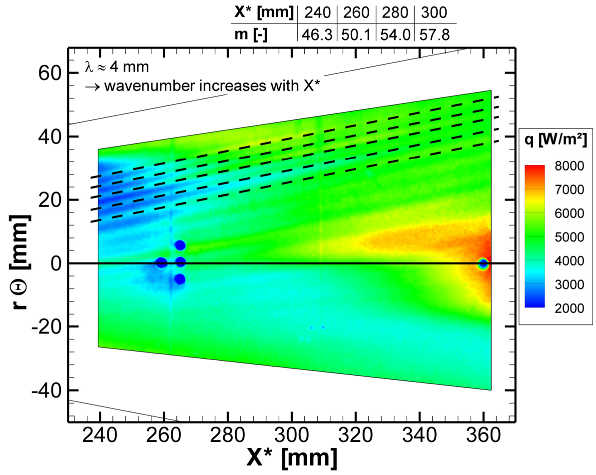

(b) present measurements

Figure 22: Comparison of crossflow wavenumber for the smooth cone between numerical computation and present measurements, numerical data taken from Balakumar (2009)

They excited fixed wavenumber stationary crossflow modes with arrays of isolated roughnesses and showed that as consequence of proper excitation exclusively the stimulated wavenumbers and its higher harmonics develop. All other wavenumbers were suppressed. This led to the idea of exciting high wavenumbers that are not as strongly amplified as the naturally developing ones and to delay transition with this approach.

In this approach it is essential that the stimulation wavenumber is higher than the most unstable one, say *m* ≈ 40-70. Furthermore the stimulation has to take place before or at the point of neutral stability. As reasonable estimate from stability computations (e.g. Balakumar (2009)) we assume that this point is at approximately *X*=50mm. There the boundary layer is very thin and also the cone circumference is only about 38mm. This leads to two problems: (i) the roughness height must be small enough to prevent bypass transition and (ii) it is difficult to place more than 70 roughness elements within 38mm.

Due to these difficulties the roughness elements were placed further downstream in previous test campaigns (Kroonenberg & Radespiel (2010a, 2010b)). There it was shown that despite of the improper disturbance position the wavenumber could be modified. The transition was not delayed, but shifted forward or it remained the same. Now some experiments were conducted with the roughness elements at the proper position. The roughness elements were cut-out of tapes with three different thicknesses (*d* = 20, 50 and 100 µm). A laser was used to cut them out with quite regular shape. The elements were circles with different diameters and spacing and a listing of the different parameters is given Table 4. Figure 23 shows exemplarily one of theses roughness cases. Even with this approach for cutting the roughness elements it was not possible to generate elements with a spacing of less than half a millimeter. Therefore only tests with a detuning to too low wavennumbers were possible.

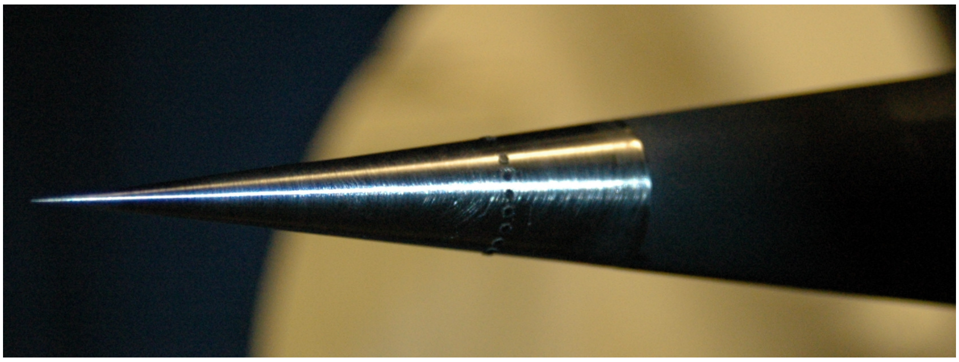

Figure 23: Photo of applied roughness elements at *X*=50mm

Table 4: Listing of different roughness properties

Case No.	Axial Position X, mm	Tape Thickness d, mm	Diameter Ø, mm	Wavenumber m, -
A	---	---	---	---
B	50 mm	0.1	1	19
C	50 mm	0.05	1	19
D	50 mm	0.05	0.75	38
E	50 mm	0.02	1	19
F	35 mm	0.05	1	13-14
G	35 mm	0.02	1	13-14
H	50 mm	0.05	2	12-13
I	50 mm	0.02	1	12
J	100 mm	0.02	1	38.5
K	100 mm	0.02	1	25.7
L	100 mm	0.02	0.7	50
M	100 mm	0.02	1	15
N	245 mm	0.1	1	94.5
O	155 mm	0.1	1	60
P	155 mm	0.1	0.75	120

Results for configuration B are given in Fig. 24. In this case the roughness diameter was 1mm with a spacing of 2mm and a thickness of ≈100µm. For the lower Reynolds number no stationary crossflow vortices were visible on the smooth cone whereas these vortices appear in the presence of roughness elements. The wavelength seems to be decreased compared to results for the smooth cone (at higher Reynolds number) and this appears reasonable for a stimulation with $m = 19$. Also for the higher Reynolds number m seems to be reduced, but the transition considerably moved forward. In this case the roughness was quite thick. Therefore this result is not astonishing. But also the roughness elements with smaller height cause premature transition as depicted in Fig. 25. There, disturbance spectra at X=257mm are shown for this roughness configuration with different thicknesses and they are compared to the case of the smooth cone. For the smooth cone there is no indication of the second mode but a very little peak at low frequency (30 kHz). Already for the 20µm roughness elements the amplitude increases for this low and also for second mode frequencies. For the thicker roughness heights this amplitude increase becomes more pronounced. Interestingly the effect is more pronounced for the 50µm than for the 100µm roughness height. Probably this is caused by deviations in the positioning of the roughness elements, i.e. the dots might have been placed at slightly different Θ-position over the cone circumference.

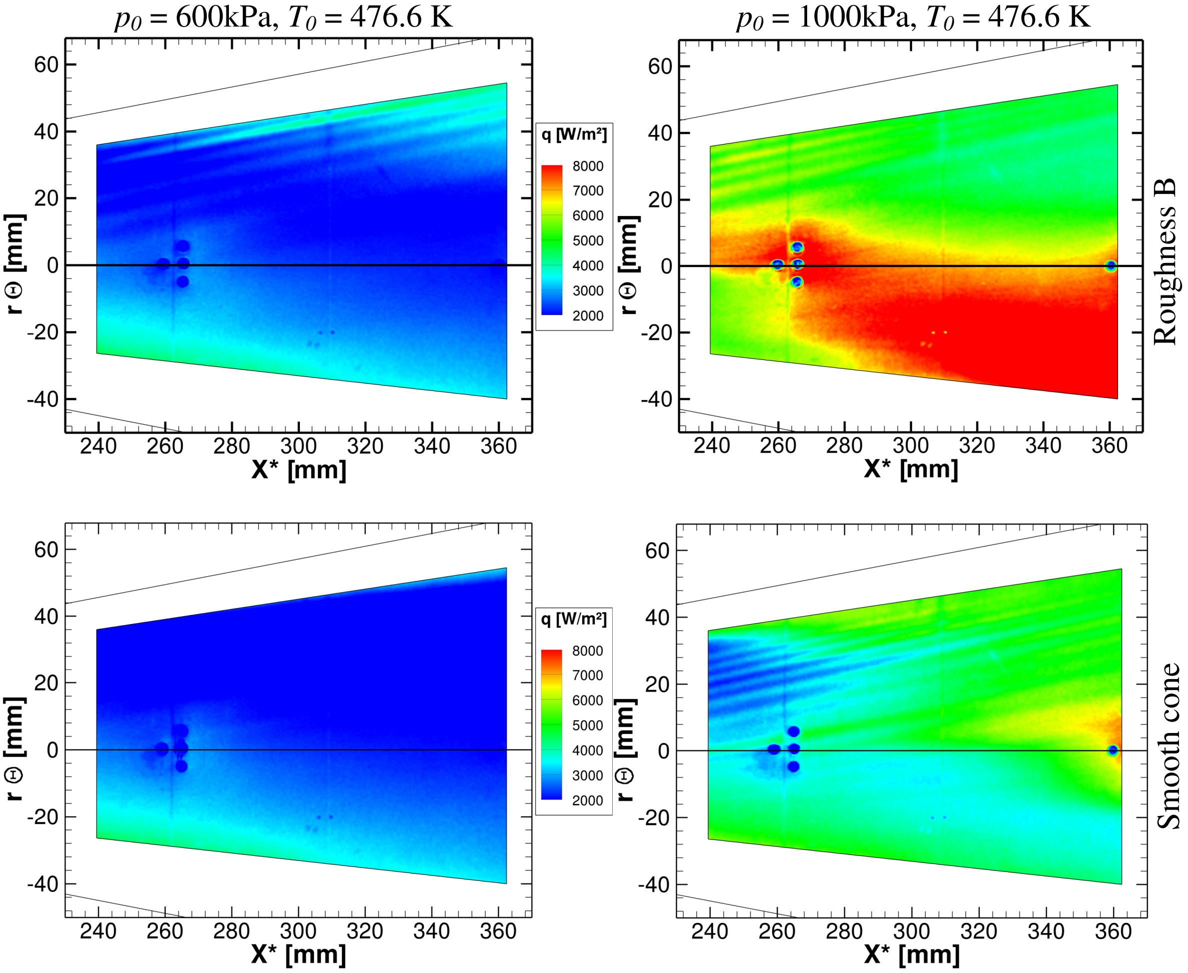

Figure 24: Comparison of heat flux between smooth cone and roughness configuration B

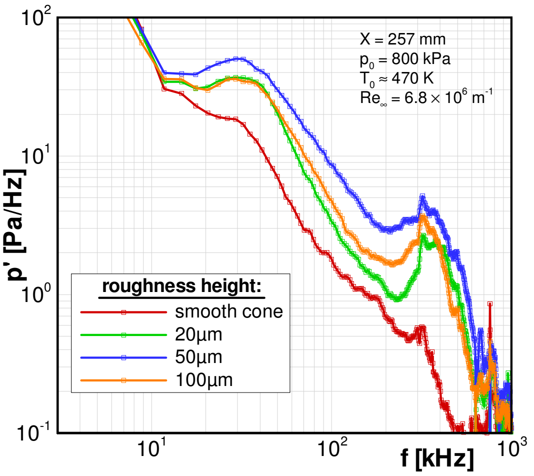

Figure 25: Disturbance spectra fort the smooth cone and in the presence of different roughness elements

As result from the preceding figures we conclude that even the 20µm roughness is too thick. It does not cause bypass transition, but the transition front moves forward and also the area where the scenario is dominated by first and/or second mode waves is enlarged. Nevertheless experiments with different roughness parameters were conducted to gain further data about possibilities for changing the wavenumber. These tests still might allow statements about the amplification of crossflow vortices with different wavenumbers although in the first and/or second mode dominated region transition moves forward.

Figure 26 shows the heat flux for two different roughness configurations and for two Reynolds numbers. In the upper row results for $Re_\infty \approx 5.0 \times 10^6\ \text{m}^{-1}$ are compared to data for the smooth cone. For the smooth cone no vortices are visible. For stimulation with m = 19 and 38 some vortices appear. The spacing between them is similar, which might be due to stimulation of harmonics in the case of m=19. In the lower row the results for the same

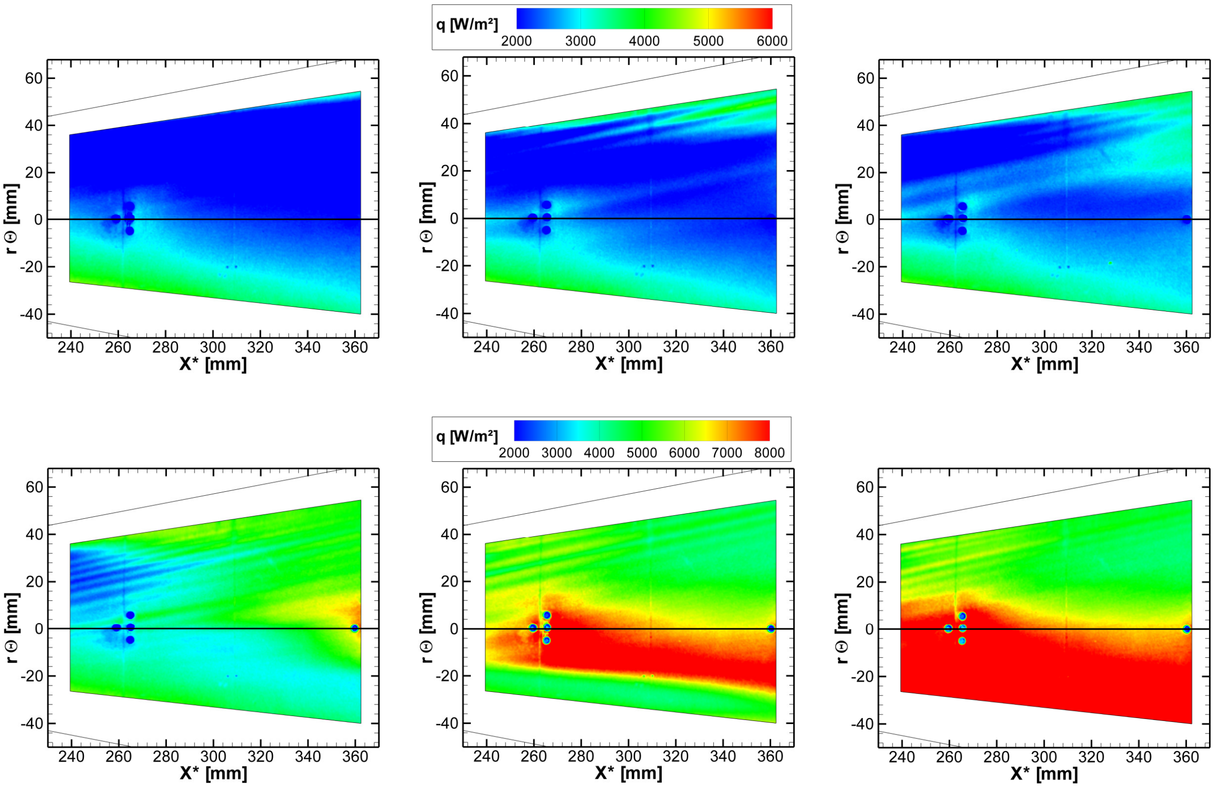

(a) smooth cone (b) m =19 (c) m = 38

Figure 26: Heat flux for stimulation with different wavenumbers, roughness at X=50mm, d=50µm, Ø0.75-1mm Flow conditions: upper row: p_0 = 600kPa, $T_0 \approx$476K; lower row: p_0 = 1000kPa, $T_0 \approx$ 476K

roughness elements but with increased Reynolds ($Re_\infty \approx 8.4 \times 10^6$ m^{-1}) number are given. Notice that the contour scale is different than for the figures in the upper row. For the smooth cone the vortices appear in the upper part whereas the transition in the lower part is first and/or second mode dominated. For m = 19 the transition front moves to the windward side, but the spacing between the crossflow vortices is increased. For m = 38 the forcing is approximately optimal and hence the transition front moves even further to the windward side. The spacing between the vortices is very similar to the smooth cone as would be expected for optimal forcing.

In one test series the diameter of the roughness elements was increased to Ø2mm to change the intensity of the induced vortices. This required a further decrease of the wavenumber to $m \approx 13.5$. The results for this series are depicted in Fig. 27 for comparison with the case m=19 in Fig. 26. The images are quite similar indicating an only marginal influence of the intensity of the artificial vortices.

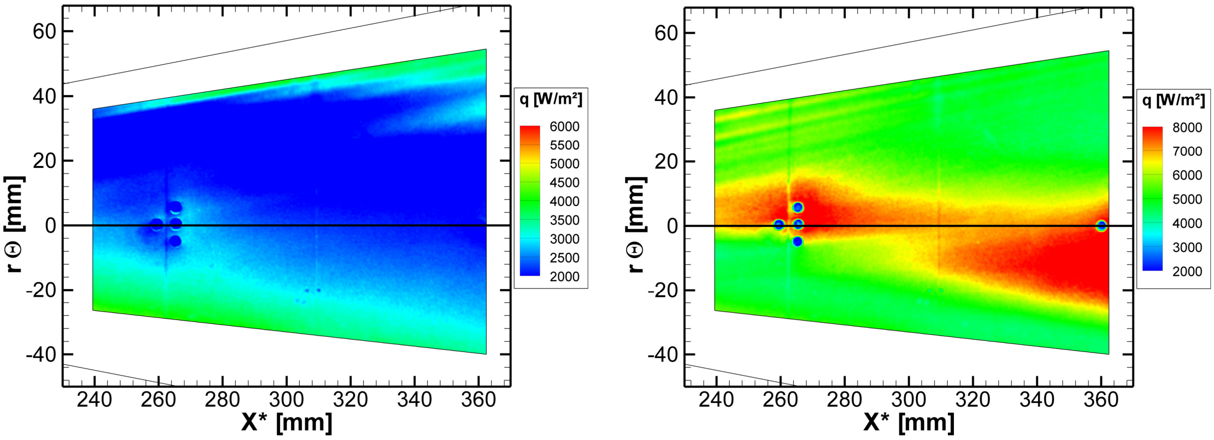

(a) p_0 = 600kPa, $T_0 \approx$476K (b) p_0 = 1000kPa, $T_0 \approx$476K

Figure 27: Heat flux for stimulation with different roughness diameter, roughness at X=50mm, d=50μm, Ø2mm Flow conditions: upper row: p_0 = 600kPa, $T_0 \approx$476K; lower row: p_0 = 1000kPa, $T_0 \approx$476K

Only a small variation of the wavenumber could be conducted when the roughness elements were placed close to the point of neutral stability. Therefore also a series with the roughness at X = 100mm was conducted and the results are given in Fig. 28. Four different wavenumbers were tested ranging from 15 to 50, i.e. all of them were either detuned to too low values or approximately the value of naturally developing vortices. In the case of low m the vortex-spacing is almost unchanged compared to the smooth cone. For medium m (25.7 or 38.5) the spacing is larger. So it seems that the approach for modifying the wavenumber also works if the roughness elements are placed after the point of neutral stability. For m = 50 the vortices seem to be spaced marginally more closely together than for the smooth cone, so increasing the wavenumber is also possible. However, the m-value is too close to the naturally developing one to produce a noticeable effect on the position of transition in the crossflow dominated region. However, a further increase of m was not possible with the applied Ø0.7 mm roughness elements.

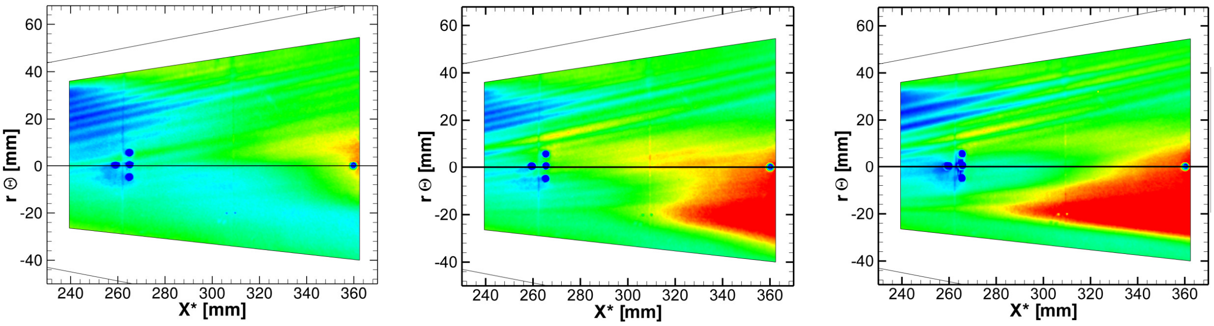

(a) smooth cone (b) m = 15 (c) m = 25.7

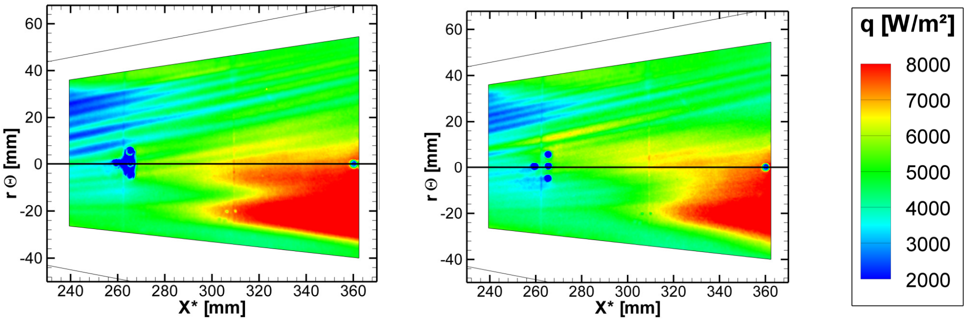

(d) $m = 38.5$ (e) $m = 50$

Figure 28: Heat flux for stimulation with different wavenumbers, roughness at X=100mm, d=20µm, Ø0.7-1mm Flow conditions: p_0 = 1000kPa, T_0 ≈476K

To increase the stimulated wavenumbers further it was necessary to place the roughness elements even further downstream. In one test series they were placed at X = 155mm with a spacing corresponding to m = 60. These results are compared to the smooth cone in Fig. 29. For the lowest Reynolds number no vortices were visible for the smooth cone. In the case of applied roughness elements the vortices appear. They develop predominantly on the windward side. This is in contrast to the case of the smooth cone where they appeared on the lee-side. This is consequence of more effective vortex-stimulation due to the thinner boundary layer on the windward side. For medium Reynolds number ($Re_\infty \approx 6.8 \times 10^6$ m^{-1}) also for the smooth cone vortices appear. This allows comparing their spacing to the case when the roughness elements are present. The vortex spacing decreased and the vortices appear also in the first and/or second mode dominated region of the model. These effects appear also for the highest Reynolds number.

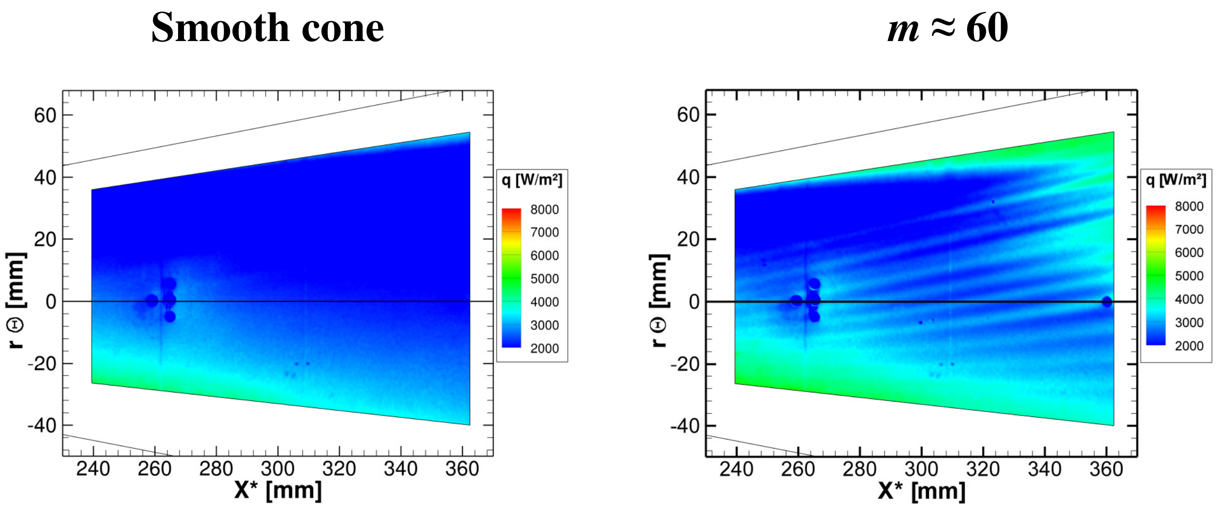

(a) $p_0 = 600$ kPa, $T_0 \approx 476$ K, $Re_\infty \approx 5.0 \times 10^6$ m^{-1}

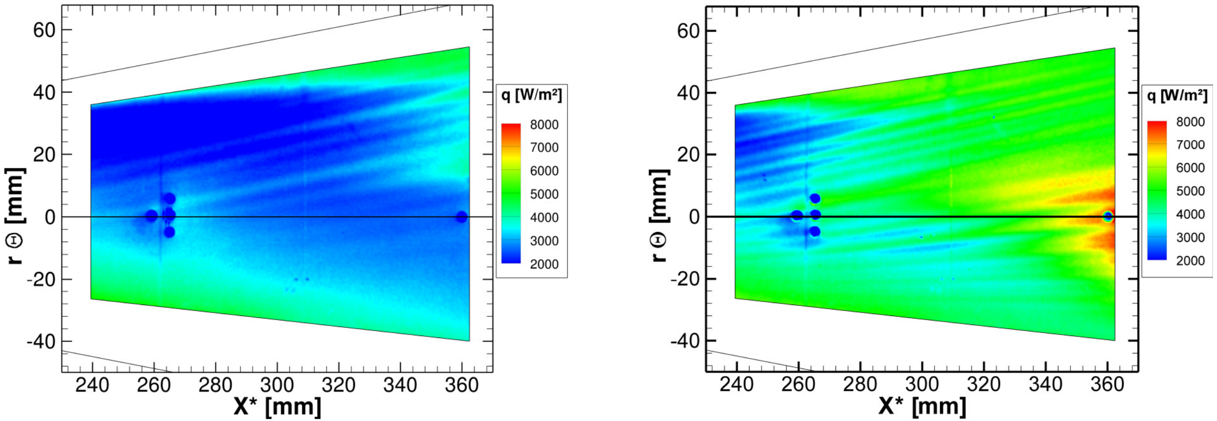

(b) $p_0 = 800$ kPa, $T_0 \approx 471$ K, $Re_\infty \approx 6.8 \times 10^6$ m^{-1}

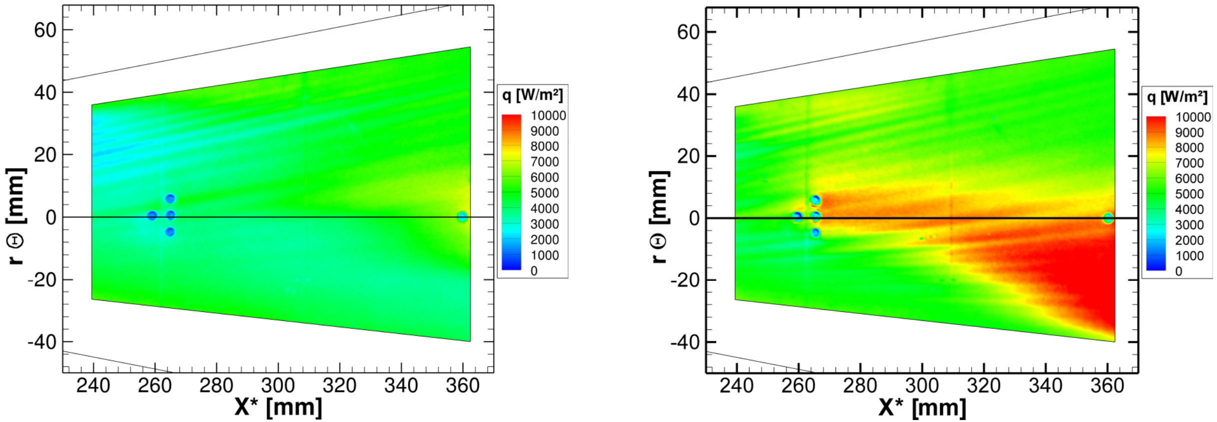

(c) $p_0 = 1000$ kPa, $T_0 \approx 476$ K, $Re_\infty \approx 8.4 \times 10^6$ m^{-1}

Figure 29: Heat flux for stimulation at a wavenumber higher than the natural one, roughness at X=155mm, d=100µm, Ø1mm

5 Conclusion

The laminar-turbulent transition on an inclined cone (6deg AOA) was investigated. Due to the inclination a 3D flow field is generated and as consequence different instability mechanisms drive the transition. While the transition on the windward side is dominated by convecting instabilities there is clear evidence for crossflow modes on the cone shoulder and on the leeward side.

In the first section results for the smooth cone obtained with IR-thermography were presented. Measurements of stationary crossflow vortices were shown and this instability was characterized concerning location, wavenumber and amplification. Furthermore numerical computations were conducted and validated by comparisons to analytical solutions and by comparisons to measured heating rates. These simulations enable calculations of the linear stability theory that are conducted at the moment. These stability calculations will help to identify the low frequency waves. So far we assume that these waves are due to the first mode instability, but this still needs to be checked by comparing to stability theory. Furthermore these computations will provide data to compare measured growth rates with.

In the second part data from surface mounted pressure sensors were shown. It was shown that depending on the location on the cone waves in two distinct frequency ranges are present. The convecting instabilities could be resolved best on the cone shoulder. One of them is in the expected frequency range of the second mode instability and one at lower frequency. The second mode waves were characterized regarding their location and their frequency content. Furthermore by using suited evaluation methods the extent of second mode waves and the orientation of the wave fronts could be determined. To the authors knowledge this is the first time that such measurements are reported for an inclined cone. Finally some data about the nonlinear phase of the transition scenario could be obtained.

The third section covered experiments that aimed on stimulating artificial crossflow modes. Although it was possible to excite these modes artificially a transition delay was not possible. This was mainly caused by too thick roughness elements that caused increased growth of first and/or second mode waves. In addition an excitation with suited wavelengths was not possible with the here applied approach for generating the vortices. A future effort should therefore make use of a different technique for stimulating the vortices. After the end of this project phase a new cone tip is presently being manufactured with small, laser-drilled holes. The diameter is about 30µm and the wavenumber is presently m=100, but also larger m-values are possible. Experiments with this new cone tip will be conducted in the near future and with this approach we hope to fulfil the aim of transition delay.

References

Balakumar, *Stability of Supersonic Boundary Layers on a Cone at an Angle of Attack*, AIAA-2009-3555, 39th AIAA Fluid Dynamics Conference, San Antonio, Texas, 2009.

Bountin, D.; Shiplyuk, A.; Maslov, A., *Evolution of nonlinear processes in a hypersonic boundary layer on a sharp cone*, Journal of Fluid Mechanics, Vol. 611, pp. 427-442, 2008.

Driest, E. R. van, *Investigation of laminar boundary layer in compressible fluids using the Crocco method*, NACA TN-2597, 1952.

Estorf, M., *Image based heating rate calculation from thermographic data considering lateral heat conduction*, Int. J Heat Mass Transfer, Vol. 49, pp. 2545–2556, 2006.

Estorf, M., *Ortsaufgelöste Bestimmung instationärer Wärmestromdichten in der Aerothermodynamik*, No. 2008-03 in ZLR-Forschungsbericht, Shaker Verlag, Technische Universität Braunschweig, ISBN: 978-3-8322-7195-4, 2008.

Estorf, M.; Wolf, T.; Radespiel, R., *Experimental and numerical investigations on the operation of the Hypersonic Ludwieg Tube Braunschweig*, 5th European Symposium on Aerothermodynamics for Space Vehicles, 2004.

Fischer, S.; Radespiel, R., *Hypersonic Transition Experiments in 3D Cone Flow with New Measurement Techniques*, Grant no. FA8655-09-1-3014, Final Report Phase 2, March. 2011a.

Fischer, S.; Radespiel, R., *Hypersonic Transition Experiments in 3D Cone Flow with New Measurement Techniques*, Grant no. FA8655-09-1-3014, Interim Report Phase 3, Sept. 2011b.

Fujii, K.; Hirabayashi, N.; Koyama, T.; Tsuda, S.; Nakagawa, M.; Itabashi, M.; Nakamura, A., *A Measurement of Instability Wave in the Hypersonic Boundary-Layer on a Sharp Cone*, AIAA-2011-3871, 41st AIAA Fluid Dynamics Conference and Exhibit, Honolulu, Hawaii, 2011.

Heitmann, D.; Radespiel, R.; Knauss, H., *Experimental Study of Mach 6 Boundary Layer Response to Laser Generated Disturbances*, AIAA-2011-3876, 41st AIAA Fluid Dynamics Conference and Exhibit, Honolulu, Hawaii, 2011.

Heitmann, D., Rödiger, T., Kähler, C.J., Knauss, H., Radespiel, R., Krämer, E., *Disturbance-Level and Transition Measurements in a Conical Boundary Layer at Mach 6*, AIAA-2008-3951, 26th AIAA Aerodynamic Measurement Technology and Ground Testing Conference, Seattle, Washington, 23-26 June 2008.

Kroonenberg, A. van den; Radespiel, R., *Hypersonic Transition Experiments in 3D Cone Flow with New Measurement Techniques*, Grant no. FA8655-09-1-3014, Interim Report Phase 1, Sept. 2009.

Kroonenberg, A. van den; Radespiel, R., *Hypersonic Transition Experiments in 3D Cone Flow with New Measurement Techniques*, Grant no. FA8655-09-1-3014, Final Report Phase 1, March. 2010a.

Kroonenberg, A. van den; Radespiel, R., *Hypersonic Transition Experiments in 3D Cone Flow with New Measurement Techniques*, Grant no. FA8655-09-1-3014, Interim Report Phase 2, Sept. 2010b.

Mack, L. M., *Boundary Layer Linear Stability Theory, Special Course on Stability and Transition of Laminar Flow*, AGARD Rept. 709, pp. 379-409, March 1984.

Mangler,W., *Zusammenhang zwischen ebenen und rotationssymmetrischen Grenzschichten in kompressiblen Flüssigkeiten*, Zeitschrift für angewandte Mathematik und Mechanik, Vol. 28, No. 4, 1945.

PCB Piezotronics, *Pressure and Force Sensors Division, Pressure Catalog*, http://www.pcb.com/contentstore/docs/PCB_Corporate/Pressure/products/Manuals/M132A31.pdf, 2009.

Saric, W.S.; Carrillo, R.B.; Reibert, M.S., *Nonlinear Stability and Transition in 3-D Boundary Layers*. Meccanica, Vol. 33, No. 5, pp. 469-687, 1998.

Schneider, S. P., *Hypersonic Laminar-Turbulent Transition on Circular Cones and Scramjet Forebodies*, Prog. Aerosp. Sci. Vol.40, pp. 1-50, 2004.

Schuele, C.Y., *Control of stationary cross-flow modes in a Mach 3.5 boundary layer using patterned passive and active roughness*, PhD thesis at university of Notre Dame, Dec. 2011.

Sims, J. L., *Tables for Supersonic Flow Around Right Circular Cones at Zero Angle of Attack*, NASA SP-3004, 1964.

Wolf, T.; Estorf, M.; and Radespiel, R., *Investigation of the starting process in a Ludwieg tube*, Theoretical and Computational Fluid Dynamics, Vol. 21, pp. 81–98, 2007.

List of Symbols, Abbreviations and Acronyms

Symbols

bi^2	bicoherence
d	thicknenn, m
f	frequency, Hz
m	wavenumber, -
p	pressure, Pa or bar
q	heat flux, W/m²
r	radius, m
M	Mach number
Re	Reynolds number
T	temperature, K
X	axial position, m
X^*	surface position, m
θ	circumferential cone angle, deg

Abbreviations

AOA	angle of attack
HLB	Hypersonic Ludwieg Tube Braunschweig
BL	boundary layer

Indices

0	initial quantity
∞	free stream
`	fluctuating quantity